Resampling method for semi-targeted continuous gravitational wa ve search in Virgo interferometer

O.Torre, S.Braccini, G.Cella, I.Ferrante, D.Passuello

VIR-0013A-10

Contents

Introduction

Many gravitational wave detectors are currently in action all around the world to detect gravitational wave signals between a few tens of Hz and a few kHz. Their sensitivity is going to be improved in the next generation of antennas, that will be soon operative.

A crucial point in gravitational wave signal search is the development of efficient algorithms to distinguish the signal from the noise in the detector output. Several astrophysical sources are expected to emit gravitational waves with different waveforms, within the ground-based antenna detection band. We will focus on one particular family of them, the *rotating neutron stars*, which is expected to permanently emit gravitational waves, mainly at the double of the rotational frequency. This type of signals requires long observation times in order to distinguish the peak at the emission frequency in the antenna signal spectrum from the incoherent noise floor, since the signal-to-noise ratio scales as the square root of the integration time.

The energy of the signal spectral peak is smeared (and thus buried in the noise) by the *Doppler phase modulation* due to the antenna motion with respect to the source and by the phase shift induced by the source rotational frequency slowing because of energy losses due to both electromagnetic and gravitational emissions. The correction to these effects requires, in general, the knowledge of the source emission frequency ν, of the *spindown* $\dot{\nu}$ and of the source sky position.

In this thesis we propose a new method to compensate for Doppler and

spindown effects that turns out to be very effective. The technique is particularly useful for sources where direction is known but emission frequency is not (*semi-targeted search*). It consists in a fast resampling of the antenna signal aimed to synchronize with a large accuracy the detector time with the source one. The antenna proper time is accelerated (or slowed down) by removing (or doubling) in a timely manner single samples of the detector digitized signal so to keep the synchronization to the source clock. The applied correction, and then the recovering of the peak in the antenna signal spectrum, is valid for all the emission frequencies, fixed a given fractional spindown $\dot{\nu}/\nu$. If the emission frequency and the spindown are unknown (as in the case of semi-targeted search), one can perform the peak energy recovery assuming different possible value of the fractional spindown and search for a peak coming out from the spectral floor. In the usual techniques this operation has to be applied for any possible value of the couple of parameters ν and $\dot{\nu}$, with a larger computational effort.

Tests of the technique have been performed for different values of source frequency, spindown, sky direction and signal sampling frequency. In all cases the antenna signal phase turned out to be "locked" to the source one with the expected accuracy of $2\pi\nu/\nu_s$, being ν_s the sampling frequency of the output signal. We have proved with additional tests that the peak amplitude recovering, corresponding to this phase locking accuracy, is the expected one. In particular, for values of ν/ν_s in the range of interest, the amount of peak amplitude losses stays below 5%, that is enough for our purposes.

The resampling method has then been applied to a selection of the first Virgo Scientific Run data. The sensitivity to the detection of continuous wave signals was studied by injecting artificial sources and by statistical analysis. A correction of the output spectrum to compensate the signal amplitude modulation due to the Earth rotation can be also considered,

using the same procedure adopted by other pipelines for continuous wave signal detection.

Chapter 1

Gravitational-wave theory

The concept of gravitational wave was introduced by Albert Einstein in order to fix the Newtonian theory of gravitation and its principle of instantaneous action-at-a-distance, which is in contrast with the notion of causality as understood in the Special Theory of Relativity.

According to Newton's theory, the gravitational field produced by a body depends on $1/r^2$, but this form does not take into account the motion of the source. General relativity fixes this problem by proposing a way to treat gravitational field very similar to the electromagnetic one. The information about the motion of a source of space-time curvature propagates at the speed of light [1].

1.1 Waves in general relativity

In the Special Theory of Relativity the *space-time interval ds* between two points is given by

$$ds^2 = -c^2dt^2 + dx^2 + dy^2 + dz^2, \tag{1.1}$$

with the usual notations. Using the Minkowski metric $\eta_{\mu\nu}$, given by

$$\eta_{\mu\nu} = \begin{pmatrix} 1 & 0 & 0 & 0 \\ 0 & 1 & 0 & 0 \\ 0 & 0 & 1 & 0 \\ 0 & 0 & 0 & -1 \end{pmatrix} \tag{1.2}$$

one can introduce the repeated index summation convention to rewrite the interval as

$$ds^2 = \eta_{\mu\nu} dx^\mu dx^\nu \tag{1.3}$$

The space-time interval is a fundamental concept in the Special Theory of Relativity because of its independence of the reference frame.

In the General Theory of Relativity Einstein introduced a new definition of inertial frame of reference by considering a mass freely falling under the gravitational attraction due to other bodies, rather than a mass not subjected to external forces. The *Equivalence principle*, or the *Universality of free fall*, states that the trajectory followed by the freely falling body is univocally determined by its initial condition (position and velocity), independently of its mass and composition. The body is seen at rest from any reference frame united to this trajectory, and the motion of any other body appears linear, if there are no other interactions besides the one due to gravitation and, as discussed in the following, if one looks at a limited space-time region. This reference frame has thus the same characteristics of a classical reference frame, in which space is homogeneous and isotropic and time is homogeneous. General Theory of Relativity is based on the extension of the principle of relativity to this class of reference frames.

The space-time region described needs to be limited, in order to guarantee the validity of the previous argument. Indeed, the effects of the force of gravity would become evident in a reference frame including a large region, because the trajectories of the freely falling masses would curve accordingly to the distribution of the sources of attraction. The more general expression

for the space-time interval takes the following form:

$$ds^2 = g_{\mu\nu} dx^\mu dx^\nu \tag{1.4}$$

where all the information about space-time curvature is encoded in the metric tensor $g_{\mu\nu}$.

The relationship between the metric tensor and a given distribution of matter is the crucial point of Gravitational theory, formally solved by Einstein equations:

$$R_{\mu\nu} - \frac{1}{2} g_{\mu\nu} R = \frac{8\pi G}{c^4} T_{\mu\nu}. \tag{1.5}$$

Eq. (1.5) is a system of sixteen equations, ten of which are independent. $R_{\mu\nu}$ is the *Riemann tensor*, a set of non-linear functions of the metric tensor and its derivatives, and it is also called *curvature tensor*, because in bidimensional varieties it reduces to a scalar which is numerically equal to the inverse of the local radius of curvature. $R_{\mu\nu}$ is null everywhere in ordinary Euclidean spaces. $R = g^{\mu\nu} R_{\mu\nu}$ is named Ricci scalar and G is the Newton gravitational constant. Thus the Einstein equations connect the mass density to the Riemann tensor through the *energy-momentum tensor* $T^{\mu\nu}$. In the limit of small density and velocity of the masses, from eq. (1.5) the classical expression for gravitational interaction is obtained:

$$\Delta\phi = -4\pi G\rho \tag{1.6}$$

where ϕ is the Newtonian potential and ρ is the mass density of the source.

On the Earth, where the gravitational field is weak, the metric can be written as a small perturbation $h_{\mu\nu}$ of the flat space-time:

$$g_{\mu\nu} = \eta_{\mu\nu} + h_{\mu\nu} \qquad\qquad |h_{\mu\nu}| \ll 1 \tag{1.7}$$

The theory based on this approximation is named *linearized gravitational theory*. Since the numerical values of the components of a tensor depend on the reference frame, we are only interested in the ones in which this

approximation holds on a sufficiently large region of space. Defining:

$$h = \eta^{\mu\nu} h_{\mu\nu} \tag{1.8}$$

and

$$\bar{h}_{\mu\nu} = h_{\mu\nu} - \frac{1}{2}\eta_{\mu\nu} h \tag{1.9}$$

and choosing the Lorentz gauge $\partial^\nu \bar{h}_{\mu\nu} = 0$, the Einstein equations reduce to [2]:

$$\Box \bar{h}_{\mu\nu} = -\frac{16\pi G}{c^4} T_{\mu\nu}, \tag{1.10}$$

where the symmetric 4×4 matrix $h_{\mu\nu}$ has only six independent components. Eq. (1.10) together with the Lorentz condition provides the conservation of energy-momentum tensor in the linearized theory:

$$\partial^\nu T_{\mu\nu} = 0 \tag{1.11}$$

The motion of a body in a gravitational field can be seen as a particular series of events in the metric space ruled by a given distribution of matter. The trajectories followed by the freely falling masses are curves defined by the geometrical characteristics of the space-time, the *geodetics*. Geodetics are curves of minimum space-time length joining two given events. The equation that describes these curves is the generalization of the equation of motion in absence of any force, i.e. when acceleration is null.

1.2 Propagation of gravitational field

A mechanisms of propagation for gravitational field similar to the electromagnetic case can be found in the linearized gravitational theory. This approximation is valid because the space-time metric tends to the flat metric when the distance from the source is large. The solution of eq. (1.10) similar to the retarded potentials in electromagnetism can be given [2]:

$$\bar{h}_{\mu\nu} = \frac{4G}{c^4} \int \frac{d^3\vec{x}'}{r} \left[T_{\mu\nu}\right]_{t-r/c}. \tag{1.12}$$

As in the electromagnetic case, non-stationary solutions have a finite velocity of propagation, carry an amount of energy and decrease with $1/r$. These solutions describe therefore gravitational waves. In empty space, far from the source, gravitational waves satisfy the following relation:

$$\Box \bar{h}_{\mu\nu} = 0 \tag{1.13}$$

that corresponds to the choice of the harmonic gauge. As in the case of electromagnetism, any solution of this equation can be written as a superposition of transverse plane monochromatic waves:

$$h_{\mu\nu}(\vec{x}, t) = h_0 \epsilon_{\mu\nu} e^{i\frac{\omega}{c}(\hat{n}\cdot\vec{x} - ct)}. \tag{1.14}$$

Everywhere the field associated to (1.14) oscillates with frequency ω and maximum amplitude h, constant over any plane orthogonal to the versor $\hat{n}$ and the quantity

$$\varphi = \frac{\omega}{c}(\hat{n}\cdot\vec{x} - ct) \tag{1.15}$$

is the phase of the wave. All the points of an equiphase surface move with velocity c towards $\hat{n}$, that can be then taken as the direction of the wave propagation. The unique difference with respect to the electromagnetic case is that now we are in presence of a tensorial field.

$\epsilon_{\mu\nu}$ is the wave polarization tensor, and it is a complex 4×4 matrix, due to the fact that the field has the same structure of the metric tensor. Although the vectorial space corresponding to a 4×4 matrix has 16 dimensions, the physically different polarization can be obtained by just two independent matrixes, while the others are the representation of the same solutions in different reference frames. In a particular gauge, named *transverse traceless gauge* (TT), the polarization tensor can be written by a transverse matrix, orthogonal with respect to the propagation direction, with a null trace (hence the name). If we apply a rotation to the three spatial axes of the TT reference frame in order to make the z axis coincident with the wave

propagation direction, any polarization can be expressed as a combination with complex coefficients of the following matrixes:

$$\varepsilon^{TT}_{\mu\nu,+} = \begin{pmatrix} 0 & 0 & 0 & 0 \\ 0 & 1 & 0 & 0 \\ 0 & 0 & -1 & 0 \\ 0 & 0 & 0 & 0 \end{pmatrix} \qquad \varepsilon^{TT}_{\mu\nu,\times} = \begin{pmatrix} 0 & 0 & 0 & 0 \\ 0 & 0 & 1 & 0 \\ 0 & 1 & 0 & 0 \\ 0 & 0 & 0 & 0 \end{pmatrix} \tag{1.16}$$

whose physical meaning will be clear in the following.

1.3 Interaction of gravitational waves with test masses

In the TT gauge, the space-time interval between two points in a gravitational-wave field propagating along the z axis with polarization ε^{TT}_{+} is given by

$$ds^2 = \left[1 + h\ \cos\left(\frac{\omega}{c}(z - ct)\right)\right] dx^2 + \left[1 - h\ \cos\left(\frac{\omega}{c}(z - ct)\right)\right] dy^2 + dz^2 - c^2 dt^2. \tag{1.17}$$

Let us consider two simultaneous events aligned along the x axis, defined by the following coordinates

$$X_{1,\mu} = (t, x, y, z) \qquad X_{2,\mu} = (t, x + L, y, z). \tag{1.18}$$

One assumes that these events are the extremes of a segment lying along the x polarization axis of the gravitational field. The infinitesimal vector oriented in the direction of this segment has only the x component different from zero:

$$dX_\mu = (0, dx, 0, 0). \tag{1.19}$$

Substituting eq. (1.19) in eq. (1.17), reminding the condition $h \ll 1$, one obtains:

$$ds = \left[1 + \frac{h}{2} \cos\left(\frac{\omega}{c}(z - ct)\right)\right] dx. \tag{1.20}$$

Integrating this expression between $X_{1,\mu}$ and $X_{2,\mu}$ the proper distance is:

$$s_{12} = \int_1^2 ds = L + \frac{Lh}{2}\cos(\omega t + \varphi). \tag{1.21}$$

A similar result, with the opposite sign (see eq. (1.17)), would be achieved for two contemporaneous events along the y axis. From these results one can state that the proper distance of a segment lying on a polarization axis (x or y) oscillates with the same frequency of the gravitational wave.

Some considerations about the physical meaning of the TT gauge are necessary. The *geodesic equation* in TT frame (eq. (1.17)) shows that, in absence of external non-gravitational forces, any trajectory in the space-time is a geodesic trajectory, i.e. it is freely falling. This means that any free mass initially at rest in the TT space remains at rest. The TT space is therefore physically represented by a system of free masses, each univocally determining a tern of spatial coordinates. The effect of a gravitational wave is then the oscillation of the proper distance between two free masses at the same spatial distance with respect to each other. In other words, the coordinates of the TT frame stretch themselves, in response to the arrival of the wave, in such a way that the spatial position of free test masses initially at rest do not change. The physical effects of a gravitational wave can be found monitoring the proper distances between the test masses.

As shown in sec. (1.2), the TT frame has the advantage that gravitational waves assume a very simple form. However, a more intuitive frame named *detector proper frame* can be used. In this particular reference frame the oscillation of the proper distance induced by a gravitational wave can be detected through the effective motion of a body in a laboratory.

Let us consider the coordinate transformation

$$\begin{cases} x' = x\left\{1 + \frac{h}{2}\cos\left[\frac{\omega}{c}(z - ct)\right]\right\} \\ y' = y\left\{1 - \frac{h}{2}\cos\left[\frac{\omega}{c}(z - ct)\right]\right\} \end{cases} \tag{1.22}$$

giving the following expression for the metric:

$$ds^2 = -c^2dt^2 + dx'^2 + dy'^2 + dz^2 - xHdtdx' + yHdx'dz - yHdy'dz \tag{1.23}$$

where $H = h\omega \sin\left[\frac{\omega}{c}(z - ct)\right]$. With this choice of coordinates, the proper distance between two contemporaneous events ($dt = 0$) aligned orthogonally with respect to the wave propagation ($dz = 0$), with both x' and y' constant in time, coincides with their Euclidean distance:

$$ds^2 = dx'^2 + dy'^2. \tag{1.24}$$

In absence of gravitational waves the new coordinate system is referable to an Euclidean space, therefore the proper distance between the two events is not affected by the transit of a gravitational waves. We can see these two events as the ends of a rigid ruler with which an observer can confront the position of a body and to measure its displacement. This process can be briefly described as follows:

1. The local inertial reference frame is defined by a freely falling mass in the field of a plane polarized gravitational wave. The test mass defines the origin of the reference frame $O_t^\mu = (t, 0, 0, 0)$;

2. A rigid ruler is located along a direction of polarization, with one of its ends coinciding with the origin O_t^μ. The other end will then define the point $X_L'^\mu = (t, L, 0, 0)$. The resulting X' axis represents the detector proper frame coordinate to which the transformation (1.22) refers.

3. At $t = 0$ a freely falling mass in $X_L'^\mu$ is put at rest with respect to the TT frame. The mass has TT coordinates $X_L^\mu = (0, L, 0, 0)$, that remains the same at any time, according to what said before about the TT frame.

4. The equation of motion of the test mass are written in the detector reference frame, that is simply the transformation of $X_L^\mu(t)$ by eq. (1.22). We obtain

$$X_L'^\mu(t) = \left(t, L\left[1 + \frac{h}{2}\cos(\omega t)\right], 0, 0\right). \tag{1.25}$$

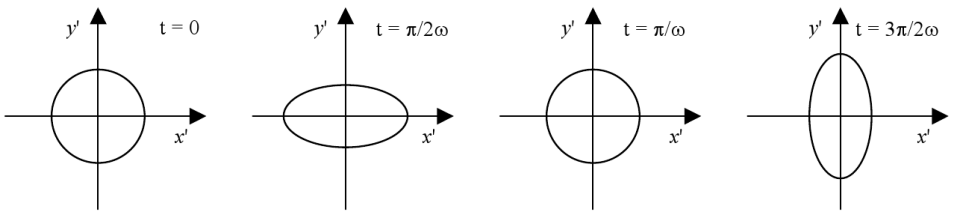

Figure 1.1: *The deformation of a ring of test masses due to the + and × polarization*

As a consequence in this reference frame an oscillation of the test mass position with respect to the ends of the ruler occurs. The oscillation frequency is equal to the one of the gravitational wave, with amplitude $Lh/2$.

A similar argument shows that if the freely falling mass is on the y axis, an oscillation with same frequency and amplitude, with a dephasing of π with respect to the one previously described, will take place. One can conclude that in the detector proper reference frame a gravitational wave gets the mass on the x axis closer to the origin and the mass on the y axis further away. The opposite effect is induced half cycle later.

The resulting deformation of a ring of test masses located in the (x, y) plane is shown in Fig. (1.1). If $\varepsilon^{TT}_{\mu\nu,\times}$ is the wave polarization, the maximum oscillation axis of the ring corresponds with the bisector of the quadrants. Indeed, the two polarizations differ only by a $\pi/4$ rotation of the reference frame around the z axis. The physical meaning of + and × polarizations defined in eq. (1.16) is now clear.

Gravitational waves are thus in principle observable as the cause of a motion of freely falling masses with respect to a rigid reference frame. This motion can be interpreted as the application of a reciprocal force between the masses produced by a gravitational field. More generally, one can state that small fluctuations of the proper distance, referred to a rigid frame, can

be interpreted in terms of a force.

Current gravitational wave detectors are based on the interferometric detection of this displacements. It is important to stress that the magnitude of this displacement is proportional not just to the gravitational wave amplitude h, but even to the distance L between the test masses.

1.4 Physics of gravitational wave generation

In order to understand how the amplitude of a gravitational wave is connected to the dynamics of the source, it is necessary to study the retarded potential solution (see eq. (1.12)) of Einstein equations in linearized theory (eq. (1.10)).

As in the electromagnetic case, a multipole expansion of the emitted signal can be made as a function of $\vec{v}/c$ (that is equivalent to state that the dimensions of the source are small with respect to the emitted wavelength). The main difference with respect to the electromagnetic case is that the first term, not necessarily null, is the equivalent of the electrical quadrupole field[1]. Taking the Taylor expansion around the parameter $\vec{v}/c$. Its spatial component can be written as

$$h^{ij}(\vec{x},t) = \frac{2G}{c^4 r_0}\left[\frac{d^2 I^{ij}}{dt'^2}\right]_{t-r_0/c} \tag{1.26}$$

where the *quadrupolar momentum* I^{ij} is defined by

$$I^{ij} = \int d^3\vec{x'}\rho(\vec{x'},t')\left(x'^i x'^j - \frac{1}{3}|\vec{x'}|\delta^{ij}\right) \tag{1.27}$$

and r_0 is the distance between the source and the point at which the field is computed. The quadrupolar momentum I^{ij} is proportional to the mass of the source, but it also depends on the asymmetry of its density. The components of I^{ij} are different from zero only if the mass distribution has

[1] The consideration of the impulse and of the angular momentum in an isolated source makes null the terms equivalent to electric and magnetic dipole emissions respectively [3].

not spheric symmetry. The gravitational-wave amplitude depends on the second derivative of I^{ij}, i.e. on the components of acceleration breaking the spherical symmetry.

The factor $G/c^4 = 8.3 \times 10^{-45}\ s^2/Kg \cdot m^2$ is responsible for the very small amplitude of gravitational emissions compared to other interaction phenomena, and therefore for the difficulties in gravitational wave detection.

It is easy to compute the field expressed by eq. (1.26) in the simple case of a system formed by two bodies of equal mass M, with dimensions much smaller than their orbital distance $2R$, rotating with velocity $\vec{v}$ around the barycenter [1]. The system emits a monochromatic wave at a frequency that is twice the orbital frequency because of the quadrupolar origin of the radiation. The direction of maximum emissivity is orthogonal to the orbital plane with an amplitude of

$$h = \frac{8GMv^2}{c^4 r_0} \tag{1.28}$$

and a circular wave polarization:

$$\varepsilon_{\mu\nu} = \varepsilon^{TT}_{\mu\nu,+} + i\varepsilon^{TT}_{\mu\nu,\times}. \tag{1.29}$$

Along the plane of the orbit the wave is + polarized, with an amplitude reduced by a factor 2 with respect to eq. (1.28).

As detailed in the next chapter, the system described above is very important, because it represents a class of objects really existing in Universe, i.e. the *binary systems*. They consist in a couple of stars rotating around each other because of the mutual gravitational attraction. Often the mass and the velocity of these systems are enough to make them gravitational wave sources of remarkable amplitudes.

In the simplest case, the masses of the two stars are equal, the orbit is circular and the velocities are non relativistic. In such a case, we can use the classical relationship between the velocity and the orbital radius for Keplerian motion can be used in eq. (1.28). This allows us to estimate the

amplitude of the gravitational field in terms of the binary system dimensions and of the distance of the observer from the source:

$$h \approx \frac{R_S^2}{r_0 R} \tag{1.30}$$

where $R_S = \frac{2GM}{c^2}$ is the *Schwarzschild radius* associated to a mass M. Its order of magnitude is of a few kilometers for masses of the same order of the Solar one. It is important to remind that the amplitude of the gravitational wave scales with the inverse of the source distance r_0.

In order to provide the order of magnitude of the expected signal, let us consider a typical binary system with dimensions comparable to those of the Solar System ($R_S \sim 10^3\ m$, $R \sim 10^{12}\ m$). This system emits a gravitational wave with frequency $\Omega \sim 10^{-9}$ Hz and amplitude $h \sim 10^{-25}$, measured over a typical galactic distance of a thousand light-years. If the binary system is composed by Neutron Stars (NS) or Black Holes (BH) in a very near orbit ($R \sim 10\ R_S$), the amplitude of the gravitational wave would be $h \sim 10^{-17}$ over galactic distance, or $h \sim 10^{-20}$ over millions of light-years, with a frequency $\Omega \sim 10^3\ Hz$. The frequency of the emitted wave is very important, because the detector sensitivity strongly depends on frequency. As we will discuss in the following, the present ground-based interferometers cannot achieve the needed sensitivity for frequencies lower than a few Hz.

In the next section we will shortly discuss the most promising astrophysical phenomena in which large amounts of matter are subjected to huge acceleration.

1.5 Astrophysical sources of gravitational waves

A variety of objects and processes in the Universe may give rise to detectable gravitational waves on Earth. Thanks to its scarce interaction with matter, gravitational waves can pass through matter without being absorbed, in spite of what happens for electromagnetic waves. This would make possible

to detect astrophysical events coming from very dense or opaque sky zones. However, the probability for these sources to be actually detected depends on many factors, as the strength of their emission, the frequency of their signal and even the number of the possible sources in a given space and time.

On the basis of current knowledge, the main astrophysical sources that should produce gravitational waves of remarkable amplitude in a frequency band accessible to ground-based interferometers (from a few Hz to a few kHz) are *compact object coalescing binaries* (Neutron Star-Neutron Star, Black Hole-Black Hole or Neutron Star-Black Hole), *Supernovae*, *rotating Neutron Stars* and *stochastic background* [4].

1.5.1 Compact object binaries

About one third of the stars in the Galactic disk is in a binary system [5]. As shown above, this kind of systems are expected to emit gravitational waves at the double of their orbital frequency. Binary systems composed by compact objects, such a couple of Neutron Stars (NS), by a couple of Black Holes (BH) or by a NS and a BH loose energy because of gravitational wave emission. This causes the progressive decrease of the orbital radius and of the orbital period. The permanence time around a given frequency (defined as $\nu/\dot{\nu}$) decreases with a strong power of the frequency itself ($\sim \nu^{-8/3}$). The two objects spend therefore millions of years orbiting at very low frequency, well below the ground-based detector sensitivity band. Only in the minutes immediately before the collision, the orbital frequency, and thus the wave emission one, increases dramatically sweeping in a few minutes the band of ground based detectors (from a few Hz to a few kHz), until it reaches its maximum frequency at the merging (around 1 kHz for NS/NS). During this phase, called *coalescence*, the system is a source of gravitational waves of remarkable intensity. Binary systems can then be detected by ground-based

interferometers only in the last minutes of their life, when the two bodies are close enough to orbit at frequencies larger than a few Hz. This is the reason why, despite the large number of compact binary systems in the close Universe, the rate of signals available for ground-based detection is low. The inspiralling signals are the most promising sources for ground-based detection. In addition to the expected remarkable amplitude an advantage is given by the fact that the dynamics of these systems is well known and its time evolution can be described as a function of a few parameters. This allows using wave templates, to be correlated with the antenna output, in order to distinguish the signal from the noise.

The only experimental proof, although indirect, of the existence of gravitational waves comes indeed from a binary system. The extended observation of the period of the *Pulsar PSR1913+16* binary system showed an inspiralling of the orbit in a strong agreement with that predicted by General Relativity because of gravitational wave emission [6]. The expected rates for NS/NS binaries for the present detectors, able to distinguish a signal over a horizon (that represents the maximum distance where this signal can be detected with a signal-to-noise ratio of at least a few units, and increases when the detector sensitivity improves) of a few tens of Mpc, range from 10^{-3} event per year to a few events per year. Advanced detectors should have a horizon of a few hundreds Mpc, and the expected rates are between a few events per year to several events per year.

1.5.2 Supernovae

The Supernova explosion in our galaxy has been a well documented event for many centuries. Both ancient and recent observations allow us to expect a few events per century, considering only Supernovae that end with the generation of a NS. Once the nuclear reactions cease, the gravity in the star is no longer balanced by the outward pressure generated by electromagnetic

radiation, and the matter starts to fall towards the center of the star. In the nucleus of the star, the extreme compression induces the collapse of the atomic structure, the fusion of proton-electron pairs into neutrons and the emission of radiation. At this point, the gravitational collapse ends abruptly, because the nucleus has reached its maximum compactness and it then turns into a Neutron Star. The huge quantity of energy released leads to the expansion of external layers and to a strong increase of the star luminosity.

Although electromagnetic emissions due to this phenomenon are very easy to detect, the gravitational wave emission could not be so large, because the gravitational collapse should be mainly spherical. In this case the acceleration of quadrupole momentum, depending on the breaking of spherical symmetry, could be very small. A Supernova is expected to emit a gravitational wave burst lasting a few millisecond with dimensionless amplitude of

$$h \simeq 2.7 \cdot 10^{-20} \left(\frac{\Delta E}{M_0 c^2}\right)^{1/2} \left(\frac{1\ kHz}{f}\right)^{1/2} \left(\frac{10\ Mpc}{r}\right) \tag{1.31}$$

where f is the characteristic frequency (i.e. the inverse of the collapse time), ΔE is the energy emitted in the form of gravitational wave, M_0 is the solar mass and r is the distance between the source and the observer. The amplitude of the emitted signal depends on the degrees of asymmetry of the collapse, giving the acceleration of the quadrupole momentum. This parameter is not predictable with enough accuracy to provide exact estimates of the rate of detectable signals. However theoretical estimates lead to the conclusion that gravitational waves produced by such events in our galaxy would be detectable even by present ground based detectors [4].

In the meanwhile, one can search for events generated in the near galaxies. The Virgo cluster is constituted by a few hundreds of galaxies, in which a few Supernovae can explode each year [7]. Unfortunately, their distance

from the Earth (about $3 \cdot 10^7$ light-years) is such that only events with very high asymmetry can be detected.

1.5.3 Rotating Neutron Stars

In our galaxy tens of millions of rotating Neutron Stars are expected to emit gravitational waves, mainly at the double of their rotational frequency, which is the frequency of the quadrupole variation. A few of them are *Pulsars*, namely sources of a regularly pulsating signal detectable in radio band. Over 1700 Pulsars have been discovered so far, and there is a population of $10^5 \div 10^6$ active Pulsars, while hundreds of millions of invisible rotating Neutron Stars are expected in our Galaxy. A blind search of continuous waves is thus necessary to discover objects that cannot be seen through their electromagnetic emissions. Most of the Pulsars have periods between 0.25 and 2 seconds, while a few Pulsars rotate at hundreds of Hz. All periods are lengthening as the Pulsars slowly lose their kinetic energy of rotation because of electromagnetic and gravitational wave emissions. For the majority of Pulsars the rotation slows down on a timescale (defined as the rate of change of their periods $P/\dot{P}$) of 10^6 to 10^8 years. The period distribution and slowdown rates suggest that most Pulsars start their lives with periods below 100 milliseconds, follow similar evolutionary paths, and cease to radiate after a few millions of years [8]. The amplitude of a gravitational wave emitted by a Pulsar expected on the Earth depends on the rotation frequency f, on the distance from Earth r and on the *ellipticity* ε. The latter is the asymmetry parameter, defined, in the simple model of an equatorial plane with an elliptical section, as $1 - a_{min}/a_{max}$, where a_{min} and a_{max} are the semi-minor and semi-major axis respectively. The expression for the amplitude is:

$$h \simeq 3 \cdot 10^{-27} \left(\frac{10kpc}{r}\right) \left(\frac{f}{200Hz}\right)^2 \left(\frac{\varepsilon}{10^{-6}}\right). \tag{1.32}$$

The signal-to-noise ratio, for a signal at a fixed frequency, goes as the square root of the integration time. Pulsars are detectable for a very long period of time, so these signals can be detected despite the fact that their amplitude is very low in comparison to that produced by other astrophysical sources. Pulsars within the limits of the ground-based detector band are expected to be around 1000 if the lower bound is 10 Hz or around 5000 if it is 5 Hz [9], amongst many other unknown rotating NS. The most promising sources for a continuous wave detection are the younger Pulsars, with high rotational frequencies. Two promising known Pulsar in the low-frequency region, where Virgo exhibits a good sensitivity, Crab and Vela. The former is a very young Pulsar with rotational frequency $\nu = 30.22$ Hz, a period of $P = 33.08$ ms and a spindown of $\dot{\nu} = -3.86 \cdot 10^{-10}$ Hz/s, while the latter has $\nu = 11.19$ Hz, $P = 89.33$ ms and $\dot{\nu} = -1.57 \cdot 10^{-11}$ Hz/s.

On a time scale of some days, all Pulsars show a remarkable uniformity of rotation rate. However, some irregularities in Pulsars rotation have been observed, producing timing irregularities such as *glitches*, that manifest themselves as remarkable step change in the rotation speed. Glitches are rare (they have been observed in fewer than 40 Pulsars), and occur more frequently in the younger Pulsars, like Crab and Vela. For example the period of the Vela Pulsar at a typical glitch (which occurs with intervals of about three years) decreases by up to 200 ns. The step change in rotational frequency typically amounts to one or two parts in 10^6 [8]. Given the rarity of the phenomenon, it will be neglected for the purposes of this discussion.

The detection of continuous waves emitted by NS is the main subject of this work. A more accurate treatment of this type of signal will follow in the next chapters.

1.5.4 Stochastic background

A broadband cosmic radiation, essentially stationary and isotropic, similarly for what happens with electromagnetic waves, is expected. This *stochastic background*, produced by cosmological process and by the sum of many unknown sources, can be described by a superposition of random gravitational signals, coming from all directions at all frequencies.

Coincidence techniques between different antennae are necessary to infer if this stochastic signal is correlated in the different detectors and to reach an acceptable sensitivity. The evaluation of the amplitude and the frequency band is very uncertain. All the astrophysical and cosmological models suggest that the amplitude of this background is very small, even if a few theoretical predictions do not exclude the possibility of a detection for advanced interferometers [10].

Chapter 2

Gravitational wave detectors

As mentioned in sec. (1.3), the gravitational wave passage induces an oscillation of the proper distance between two free masses with an amplitude that is proportional to their distance. A gravitational wave detector can be thus a system of free masses, mutually unbounded, at a very long distance from each other. This kind of arrangement is adopted by interferometric detectors.

The idea of interferometric detection of gravitational waves was first introduced by the Russian theorists M. Gertsenshtein and V. I. Pustovoit in 1962. It was also considered by Weber, and then published in the late 1960s by R. Forward, R. Weiss, R. Drever and others [11]. The complexity of the design of a long arm gravitational wave interferometer required large international collaborations and over thirty years of preparation to put them in action.

The most simple setting from which we can start to explain this kind of detectors is the Michelson interferometer.

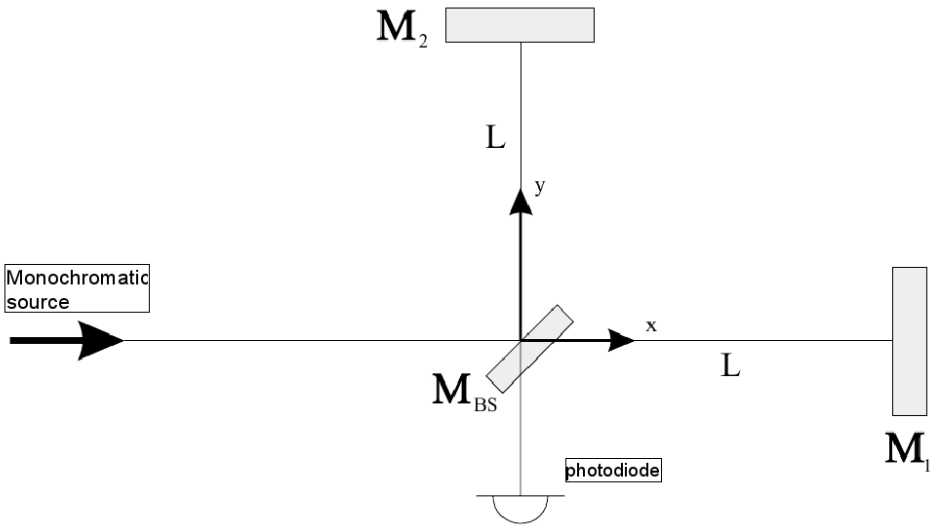

Figure 2.1: *Scheme of a Michelson interferometer for gravitational waves detection [12]*

2.1 Michelson interferometer

The Michelson interferometer is a very accurate instrument to measure changes in the travel time of light in its arms, and it was first developed by Michelson and Morley in 1887 to measure the speed of the supposed "ether wind" on the Earth surface [1].

The conceptual scheme, that we are going to remind, is shown in Fig. (2.1). It consists of a monochromatic light source, whose light hits the beam-splitter, a partially reflecting mirror inclined with an angle of 45°, that separates the beam in two equal and coherent beams travelling in the two orthogonal arms. Totally reflecting mirrors put at the end of each arm send the beams back to the beam-splitter. Part of the resulting beam goes to a photodetector that measure its intensity, while the remaining part goes back towards the laser. In a gravitational wave detector the mirrors are suspended at the end of a pendulum, and can be treated as freely falling masses as long as the pendulum frequency is much lower than the signal

frequency.

We can write a given spatial component of the electric field of the input laser light as

$$E_0 e^{-i\omega_L t + i\vec{k}_L \cdot \vec{x}} \tag{2.1}$$

where ω_L is the laser frequency and $\vec{k}_L = \omega_L/c$ is its wave vector. Denoting by L_x and L_y the length of the two arms, one can find that the power measured by the photodetector is [1]:

$$|E_{out}|^2 = E_0^2 \sin^2[k_L(L_y - L_x)] \tag{2.2}$$

The amplitude of the light that leaves the interferometer depends thus on the phase difference cumulated by the light travelling in the two arms $k_L(L_y - L_x)$. When this difference is null the light at the output has amplitude E_0 (*constructive interference*), while for $k_L(L_y - L_x) = \frac{\pi}{2}$ all the light would be reflected back to the laser source, and there would be no light at the output (*destructive interference*). Therefore any variation in the arm length difference corresponds to a variation of the power at the photodetector.

2.2 Response of a Michelson interferometer to gravitational waves

In the TT gauge description, the coordinates of the mirror and of the beamsplitter are not affected by the passage of the wave. The TT frame results then very helpful to describe the detector response, which is proportional to the arm path difference. We are therefore interested in writing the expression of the total power at the photodetector for the TT frame.

Let us consider for simplicity a plus-polarized gravitational wave in the $z = 0$ plane of the interferometer, perpendicular to the interferometer plane. The space-time interval in the TT frame is

$$ds^2 = -c^2dt^2 + [1 + h_+(t)]dx^2 + [1 - h_+(t)]dy^2 + dz^2. \tag{2.3}$$

A ray of light connects sets of points separated by $ds^2 = 0$, so along the x axis the interval between two near events connected by the light beam is given by:

$$\begin{aligned} ds^2 = 0 &= g_{\mu\nu} dx^\mu dx^\nu \\ &= (\eta_{\mu\nu} + h_{\mu\nu}) dx^\mu dx^\nu \\ &= -c^2 dt^2 + (1 + h_+(t)) dx^2. \end{aligned} \tag{2.4}$$

The square root of eq. (2.4), in the linearized approximation ($h_+ \ll 1$), gives

$$dx = \pm c dt \left[1 - \frac{1}{2} h_+(t) \right] \tag{2.5}$$

where the plus sign holds for the travel from the beam-splitter to the mirror and the minus sign for the opposite sense of the travel. If t_0 is the time at which a photon leaves the beam-splitter, the time of arrival t_a after a round trip along the x arm can be obtained by integrating eq. (2.5) over one round trip along the x arm:

$$t_a - t_0 = \frac{2L_x}{c} + \frac{1}{2} \int_{t_0}^{t_a} d\tau h_+(\tau). \tag{2.6}$$

One can approximate the upper limit of the integral as $t_a \simeq t_0 + 2L_x/c$, so, according to [11], we get

$$t_a - t_0 = \frac{2L_x}{c} + \frac{L_x}{c} h \left(t_0 + \frac{L_x}{c} \right) \frac{\sin(\omega_{gw} L_x/c)}{(\omega_{gw} L_x/c)} \tag{2.7}$$

where

$$h(t_0 + L_x/c) = h_0 \cos[\omega_{gw}(t_0 + L_x/c)] \tag{2.8}$$

is a plus polarized wave, function of the retarded time $t_0 + L_x/c$ which approximates at the first order the time t' at which the photon touches the mirror. The quantity $t_0 + \frac{L_x}{c}$ is, to zeroth order in h_0, the time at which the beam reaches the far end of the x arm. A similar expression can be obtained for the y arm:

$$t_a - t_0 = \frac{2L_y}{c} - \frac{L_y}{c} h \left(t_0 + \frac{L_y}{c} \right) \frac{\sin(\omega_{gw} L_y/c)}{(\omega_{gw} L_y/c)}. \tag{2.9}$$

Since we are interested in the light that comes out from the beam-splitter at a given time t, it is useful to invert the previous expression fixing the value of $t_a \equiv t$ and replacing $h(t_0 + L_x/c)$ by $h(t - L_x/c)$. The time at which the light started its round-trip travel is thus given by

$$t_0^{(x)} = t - \frac{2L_x}{c} - \frac{L_x}{c} h\left(t - \frac{L_x}{c}\right) \mathrm{sinc}(\omega_{gw} L_x/c) \tag{2.10}$$

and similarly for the y arm

$$t_0^{(y)} = t - \frac{2L_y}{c} + \frac{L_y}{c} h\left(t - \frac{L_y}{c}\right) \mathrm{sinc}(\omega_{gw} L_y/c). \tag{2.11}$$

The phase of the field is conserved during the free propagation, therefore setting the origin of the coordinate system at beam-splitter and writing the electric field of the light as in eq. (2.1) we see that the phase of the light at the beam-splitter at the time $t_0^{(x)}$ is $e^{-i\omega_L t_0^{(x)}}$. The expression for the electric fields that go through the two arms at a time t is then:

$$E^{(x)}(t) = -\frac{1}{2} E_0 e^{-i\omega_L t_0^{(x)}} = -\frac{1}{2} E_0 e^{-i\omega_L (t - 2L_x/c) + i\Delta\phi_x(t)} \tag{2.12}$$

$$E^{(y)}(t) = \frac{1}{2} E_0 e^{-i\omega_L t_0^{(y)}} = \frac{1}{2} E_0 e^{-i\omega_L (t - 2L_y/c) + i\Delta\phi_y(t)} \tag{2.13}$$

where

$$\Delta\phi_x(t) = h_0 \frac{\omega_L L_x}{c} \mathrm{sinc}\left(\frac{\omega_{gw} L_x}{c}\right) \cos\left[\omega_{gw}\left(t - \frac{L_x}{c}\right)\right] \tag{2.14}$$

and

$$\Delta\phi_y(t) = -h_0 \frac{\omega_L L_y}{c} \mathrm{sinc}\left(\frac{\omega_{gw} L_y}{c}\right) \cos\left[\omega_{gw}\left(t - \frac{L_y}{c}\right)\right] \tag{2.15}$$

Being L_x and L_y made as close as possible, we can replace them in the latter expressions by $L = (L_x + L_y)/2$, obtaining

$$\begin{aligned} \Delta\phi_x(t) = -\Delta\phi_y(t) = h_0 k_L L \mathrm{sinc}\left(\frac{\omega_{gw} L}{c}\right) \cos\left[\omega_{gw}\left(t - \frac{L}{c}\right)\right] \\ \equiv |\Delta\phi_x| \cos(\omega_{gw} t + \alpha) \end{aligned} \tag{2.16}$$

where $\alpha = -\omega_{gw}L/c$ is a phase. The total phase difference induced by a gravitational wave in the Michelson interferometer is then

$$\Delta\phi_{Mich} = \Delta\phi_x - \Delta\phi_y = 2\Delta\phi_x \tag{2.17}$$

The total electric field at the output is

$$E_{tot}(t) = E^{(x)}(t) + E^{(y)}(t) = -iE_0 e^{-i\omega_L(t-2L/c)} \sin[\phi_0 + \Delta\phi_x(t)] \tag{2.18}$$

where $\phi_0 = k_L(L_x - L_y)$ still takes into account any small difference between the length of the two arms. In the limit $\omega_{gw}L/c \ll 1$, i.e. when the signal frequency is smaller with respect to the inverse round trip time, a gravitational wave is nearly constant while the light makes a complete round trip in the arm. In this case eq. (2.16) reduces to

$$\Delta\phi_{Mich} \simeq 2h\left(t - \frac{L}{c}\right) k_L L. \tag{2.19}$$

The gravitational wave induces a shift between the interfering beams proportional to the wave vector and to the arm length. In the TT gauge the position of the mirrors does not change at the arrival of a gravitational wave, that affects only the propagation of light between the mirrors. In the proper detector frame, it was shown that a reversed situation takes place, i.e. the mirror position relative to a rigid ruler would change, while light propagation would not. The dephasing computed above is a relativistic invariant, i.e. its value does not change in different reference frames. This means that the effect of gravitational waves can be seen either as a change of the travelling time of the beam between the mirrors or as a change in their relative distance. The effect of the gravitational wave in the phase shift is equivalent to a change of $L_x - L_y$ given by

$$\frac{\Delta(L_x - L_y)}{L} \simeq h\left(t - \frac{L}{c}\right). \tag{2.20}$$

The total power $P \sim |E_{tot}^2|$ observed at the photodetector is modulated by the gravitational wave signal as follows:

$$P = \frac{P_0}{2}\left[1 - \cos(2\phi_0 + \Delta\phi_{Mich}(t))\right] \tag{2.21}$$

and we want then $\Delta\phi_{Mich}$ to be as large as possible. As it can be seen from eq. (2.16), its dependence on L is given by the factor

$$(\omega_L L/c)\mathrm{sinc}(\omega_{gw}L/c) = (\omega_L/\omega_{gw})\sin(\omega_{gw}L/c). \tag{2.22}$$

One can see that when the wave frequency coincides with the permanence time of the light the effect is null. Thus the optimal arm length to detect a GW of frequency $f_{gw} = \omega_{gw}/2\pi$ is given by

$$L = \frac{\pi}{2}\frac{c}{\omega_{gw}} = \frac{\lambda_{gw}}{4} \simeq 750km\left(\frac{100Hz}{f_{gw}}\right). \tag{2.23}$$

The signal received by the detector is determined by the *pattern functions* $F_+(\theta,\phi)$ and $F_\times(\theta,\phi)$, which depend on the wave propagation direction $\hat{n} = (\theta,\phi)$, as follows:

$$h(t) = F_+(\theta,\phi)h_+(t) + F_\times(\theta,\phi)h_\times(t). \tag{2.24}$$

The pattern functions, giving the response of the antenna to a given source, depend on time since the orientation of the antenna with respect to the source change because of Earth rotation. $h_+(t)$ and $h_\times(t)$ are given by

$$h_+(t) = h_{0,+}\cos(\omega_{gw}t) \tag{2.25}$$

$$h_\times(t) = h_{0,\times}\cos(\omega_{gw}t + \alpha), \tag{2.26}$$

being $h_{0,+}$ and $h_{0,\times}$ the real amplitudes for the two polarizations, and α their relative phase. The response of an interferometric antenna to the two polarization states h_+ and $h_\times$ for gravitational signals coming from an arbitrary direction (θ, ϕ) with respect to the normal to the interferometer plane

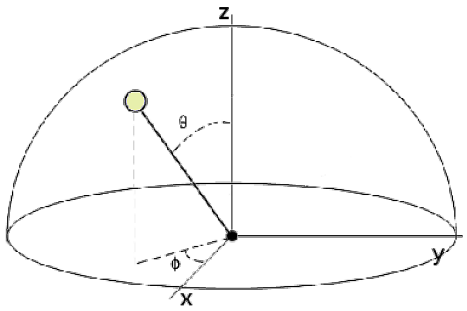

Figure 2.2: *Incident angles of the interferometer (θ and ϕ).*

(Fig. (2.2)) can be evaluated by easy geometrical considerations. In particular, the variation of the arm length ΔL induced by the two polarization states + and $\times$ is:

$$\Delta L(t) = \frac{1}{2} h_+(t) L (1 + \cos^2\theta) \cos 2\phi \tag{2.27}$$

$$\Delta L(t) = \frac{1}{2} h_\times(t) L \cos\theta \sin 2\phi \tag{2.28}$$

Fig. (2.3) provides a representation of the antenna response to unpolarized gravitational waves as a function of the incident direction with respect to the $x-y$ interferometer arms. One can notice that, apart from special directions of the interferometer plane(the two bisectors), the response of the antenna for the different directions does not change too much.

2.3 Folded interferometer arms

As one can see from eq. (2.23) the optimal arm-length to measure gravitational waves with frequencies of order of a few hundreds Hz would be of several hundreds of kilometers. Being this impossible in practice for Earth-based interferometers, the needed arm-length is therefore obtained by folding the optical path of light, making it "bounce" back and forth many times in each arm, before the interference. In Virgo, each arm of the interferometer is a 3 km long Fabry-Perot cavity resonating at the laser frequency (the

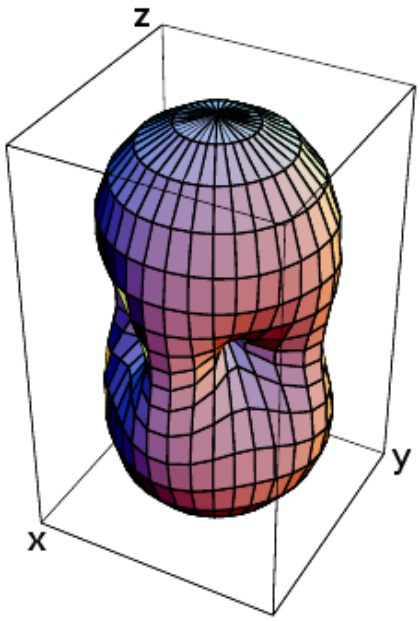

Figure 2.3: *Antenna response function to unpolarized waves for an interferometric gravitational wave detector. Interferometer arms are oriented along the box horizontal axes.*

antennas of the US LIGO project have 4 km long arms).

2.3.1 Fabry-Perot cavities

An ideal Fabry-Perot resonator (see [1]) consists of two plane mirrors separated by a distance L. Each mirror is characterized by the ratio of reflected optical field to the incident field, the *amplitude reflectivity* r and the *amplitude transmissivity* t. A beam of monochromatic light with electric field amplitude E_0 normally hits on the first mirror (that has reflectivity r_1 and transmissivity t_1), and it is partly reflected outside the cavity and partly transmitted towards the second mirror (with reflectivity r_2 and transmissivity t_2) with an amplitude which depends on the above mentioned coefficients. The cavity is said to be at *resonance* when the maximum power emerges, i.e. when $2kL = 2n\pi$, with n any integer. In this situation the phase relation

between the beams is adjusted so that they interfere in a constructive way inside the cavity. Far from resonance, just a little fraction of light is trapped inside the cavity, so most part of the incident beam is reflected off the first mirror. When the cavity is tuned precisely at resonance, the electric field in the cavity is high. Let us consider the simple case of a perfectly reflecting far mirror with $r_2 = 1$. One can write the amplitude of the light incident on the first mirror from inside the cavity as

$$E_{inside} = E_0 \frac{t_1}{1 - r_1 e^{-i2kL}} \tag{2.29}$$

Only a fraction $t_1 \ll 1$ of this field escapes from the first mirror, and since resonance occurs when $kL \approx n\pi$, which means $e^{-i2kL} \approx 1$, an approximated expression for the escaping electric field E_{esc} can be given:

$$E_{esc} = E_0 \frac{t_1^2}{1 - r_1(1 - i2kL)} \tag{2.30}$$

The real part of E_{esc} is approximately equal to $E_0(1 + r_1)$. This means that the reflected part of the electric field can be evaluated by the following expression:

$$E_{refl} \equiv -E_0 r_1 + E_{esc} \approx E_0(-r_1 + 1 + r_1) = E_0 \tag{2.31}$$

This means that the superposition of the escaping light with the promptly reflected light gives a beam with electric field amplitude E_0, as in the off-resonance case, but the escaping light has a change of phase of 2π nearby the resonance. The change in the phase of the escaping light with the cavity length L in the Fabry-Perot cavity can be seen as a particular case of a *delay line* scheme. In a delay line the beam goes back and forth inside the arms, as in a Fabry-Perot cavity. In this case, however, the mirrors are large because the light beams have to be spatially separated in order to avoid spurious interferences. In a delay line the phase variation $\partial\phi$ produced by a length variation ∂L_{DL} is given by

$$\partial\phi / \partial L_{DL} = 2N2\pi/\lambda, \tag{2.32}$$

where N is the number of round trips of the length. For a Fabry-Perot cavity this expression becomes

$$\frac{\partial\phi}{\partial L_{FP}} = \frac{4r_1}{1-r_1}\frac{2\pi}{\lambda}. \tag{2.33}$$

As a consequence a Fabry-Perot cavity has the same effect of a delay line in amplifying the phase shift due to a length variation, with $N = \frac{2r_1}{1-r_1}$. Since the beams in the Fabry-Perot cavity are superposed, the mirrors used for it are much smaller than those for a delay line, and then more convenient from many points of view (physical characteristics, cost, engineering).

The *finesse* F, defined as

$$F = \frac{\pi\sqrt{r_1 r_2}}{1-r_1 r_2} \tag{2.34}$$

is a parameter that characterizes the sharpness of the resonance of a Fabry-Perot cavity. If $r_2 = 1$ it is immediate to see that

$$F = \frac{\pi\sqrt{r_1}}{1-r_1} \tag{2.35}$$

In the limit that the time scale for metric changes is long compared with $\frac{FL}{c}$, a Fabry-Perot cavity gives $\frac{2F}{\pi}$ times the phase shift of a one-bounce interferometer arm in response to a gravitational wave [1].

2.3.2 Gaussian beams

In the previous section any dependence of the electric field on the transverse coordinates was neglected. In the realistic case of mirrors with finite transverse extent the beam, which has itself a profile in the transverse direction, is subjected to diffraction. This phenomenon causes the broadening of the beam and its dispersion on a region of transverse size larger than the mirrors (see [11]).

After traveling a longitudinal distance x the beam becomes larger, in the transverse direction, by $x\Delta\theta \sim \frac{x\lambda_L}{a}$, where a is the beam transverse width

and λ_L is the wavelength of its photons. If $\frac{x\lambda_L}{a} \ll a$ we are in the regime of *Fresnel diffraction*, and the broadening of the beam is negligible. If $\frac{x\lambda_L}{a} \gg a$ we are in the regime of *Fraunhofer diffraction*, and the broadening is not negligible anymore. For typical gravitational interferometer laser beams this means that the beam would widen remarkably already after a single one-way trip through the cavity. This problem can be avoided by using a Gaussian beam instead of an ideal plane wave. This beam has a Gaussian profile in the transverse direction. Its profile stays Gaussian for any x, and its width is a function of x:

$$w(x) = w_0\sqrt{1 + \frac{x^2}{b^2}} \tag{2.36}$$

where w_0 is the initial transverse size and $b = \frac{1}{2}k_L w_0^2$ is said *Rayleigh range*. The wavefronts of a Gaussian beam are spherical to an excellent approximation. The curvature radius, i.e. the radius of the spherical equiphase plane, depends also on x by

$$R(x) = x + \frac{b^2}{x} \tag{2.37}$$

Gaussian beams are very useful in the construction of gravitational wave interferometers because they have the minimum possible spreading. If the surfaces of mirrors match exactly the beam equiphase surfaces, this does not widen further each time it bounces between the two mirrors. Spherical mirrors are thus the optimal choice. When the beam travels back and forth between such spherical mirrors, its wavefronts are forced to converge back towards the waist, so the transverse size of the mirror does not increase.

2.3.3 Detection at the dark fringe

As shown above, the passage of a gravitational wave in an interferometer produces a phase shift proportional to the signal waveform $h(t)$ (see eq. (2.16)). The detection of gravitational waves can thus be obtained by extracting this phase from the output of the detector.

In order to maximize the instrument sensitivity, one could choose as an operating point the maximum of $dP_{out}/d\phi$. However, since we use the output power as a measure of the phase, it is not possible to distinguish a change in ϕ due to a gravitational wave from a fluctuation of the laser power. In the point of maximum $dP_{out}/d\phi$ the photodetector measures a large power even in absence of gravitational waves, and this large DC contribution has the same low frequency as the one of the perturbation of space-time due to gravitational waves.

It is a better choice to work at a point where the instrument records zero output in absence of signal, i.e. where the interferometer can be treated as a *null instrument*. To have this condition it is necessary to work at the dark fringe (see [1], [11]). This is in fact the only point where the output is zero in absence of gravitational waves and there is no sensitivity to fluctuations of the laser power. Since $dP_{out}/d\phi = 0$ the change in the output power induced by the gravitational wave is very small as well. The problem can be solved applying a *phase modulation* to the input laser light, by passing the incident beam through a Pockels cell. This causes the beam phase to change with time, and then the signal acquires sidebands. The light incident on the beam-splitter is thus composed by a carrier at the laser frequency ω_L and two sidebands at $\omega_L \pm \Omega_{mod}$ (as shown below, higher sidebands can be neglected for small phase modulation). The cavity length L is chosen so that the carrier is resonant, while the modulation frequency Ω_{mod} is fixed so that the sidebands are not resonating. The electric field incident to the beam splitter has the form

$$E_{in} = E_0 e^{-i(\omega_L t + \Gamma \sin \Omega_{mod} t)} \tag{2.38}$$

where Γ is called the *modulation index*. E_{in} can be expanded as

$$E_{in} = E_0[J_0(\Gamma)e^{-i\omega_L t} + J_1(\Gamma)e^{-i(\omega_L+\Omega_{mod})t} - J_1(\Gamma)e^{-i(\omega_L-\Omega_{mod})t} + \cdots], \tag{2.39}$$

where J_n are the *Bessel functions* of the first kind. The effect of the phase modulation is to generate sidebands. For small Γ, this expression is simply obtained expanding (2.38) in powers of Γ. Higher sidebands are then negligible. On the dark fringe, in the presence of a gravitational wave, the electric field of the carrier at the photodetector shifts from the value $(E_{out})_c = 0$ to the value

$$(E_{out})_c = -i(1-\sigma)E_0 J_0(\Gamma) e^{-i\omega_L t + 2ik_L l} \cdot \frac{2F}{\pi} k_L L h(t), \tag{2.40}$$

where J_0 is the order 0 Bessel function and $-(1-\sigma) = R$ is the reflectivity of the cavity at the resonance for k_L. The modification of the electric field due to the sidebands is negligible, since it gives a correction $1 + O(h)$, but its term $O(1)$, beating against the term $O(h)$ in the carrier, gives a term linear in h in the output. The total electric field at the output is then

$$(E_{out})_{tot} = -2iE_0 e^{-i\omega_L t + 2ik_L l} \cdot \left[(1-\sigma) J_0(\Gamma) \frac{F}{\pi} k_L L h(t) - J_1(\Gamma) \cos(\Omega_{mod} t - \alpha) \right] \tag{2.41}$$

Taking the modulus squared, the term which oscillates as $\cos(\Omega_{mod} t - \alpha)$ is linear in h and it is demodulated by a mixer. An output that is linear in $h(t)$ is thus obtained, even if the carrier is on the dark fringe.

2.4 Noise sources

The output of a gravitational wave detector is a time series which describes the phase shift of the light recombined after travelling in the two interferometer arms. This output will be a combination of a gravitational wave signal ($h(t)$) and of noise ($n(t)$). Let us consider an additive model for the output, that can thus be written as $s(t) = h(t) + n(t)$. The noise sources affecting the sensitivity of an interferometric detector can be generically divided in three classes [13]:

- *displacement noise*;
- *optical readout noise*;
- *phase noise.*

Some noise processes can generate spurious signals in the apparatus inducing a real displacement of the interferometer optical components (*displacement noise*). Other processes affect only the phase of the light beams even if a real movement of the mirrors is not present (*phase noise*). The main sources of displacement noise are the thermal noise and the seismic noise, while phase noise arises from many optical processes such as the frequency fluctuations of the laser and the refraction index fluctuations of the residual gas in the pipes. In both cases, noise mechanisms induce fluctuations of the phase of the interfering beams. These fluctuations cannot be described by deterministic laws, but are characterized only by their statistical features.

A random variable X of a system, fluctuating around its rest position, is characterized by its spectral density

$$S_X(f) = < \lim_{T\to\infty} \frac{2}{T} |\hat{X}_T(f)|^2 > \tag{2.42}$$

where $\hat{X}_T(f)$ denotes the Fourier transform of the function $X(t)$ inside the integration range $-T < t < T$ and the braket indicates the *ensemble* average. In order to define the antenna sensitivity one has to compare the expected gravitational signal $h_{gw}(t)$ with each significant spurious signal. The most suitable way to compare noise and signal is to consider each spurious fluctuation of the interference phase as produced by a *fake* signal characterized by an equivalent dimensionless amplitude $h_{noise}(t)$. The comparison between the real signal and each fake signal is usually expressed in terms of their *linear spectral density*, defined as the square root of the spectral density and indicated with $\tilde{h}_{gw}(f)$ and $\tilde{h}_{noise}(f)$, respectively (expressed in units of $Hz^{-1/2}$). As shown above, the Fabry-Perot cavities increase the dephasing

produced by displacements by a factor $\frac{2F}{\pi}$, so as long as displacement noise is dominating there is no advantage in increasing the cavity finesse, because noise would be amplified just like the signal. On the contrary, shot noise (that is a component of the optical readout noise) and phase noise are not modified by the presence of Fabry-Perot cavities, so using them is effective to amplify the phase shift in the interference beams produced by the signal, and thus increase the signal-to-noise ratio where the detector sensitivity is limited by these noise sources.

The linear spectral density of the total noise in the antenna can be obtained by the uncorrelated sum of the linear spectral densities of all the n noise contributions, namely

$$\tilde{h}_{noise}(f) = \sqrt{\tilde{h}_1^2(f) + \tilde{h}_2^2(f) + \tilde{h}_3^2(f) + ... + \tilde{h}_n^2(f)}. \tag{2.43}$$

The sensitivity curve of a gravitational wave antenna is usually expressed by plotting this quantity as a function of the frequency. Straight from the definition, it can be computed the signal to noise ratio for an impulsive gravitational signal of length τ and amplitude h. Supposing a bandwidth of the wave equal to $\Delta f = 1/\tau$, the signal-to-noise ratio is given by

$$\frac{S}{N} = \frac{h\sqrt{\tau}}{\tilde{h}_{noise}(\Delta f)} \tag{2.44}$$

where $\tilde{h}_{noise}(\Delta f)$ is the mean of the linear spectral density of the noise inside the signal bandwidth and h is the pulse amplitude. By imposing $S/N \geq 1$, it can be obtained the minimum dimensionless amplitude detectable by the antenna for a τ long impulsive gravitational signal. For a periodic gravitational signal the spectrum is very narrow, being entirely concentrated, apart from harmonics, around the fundamental frequency f_0. The bandwidth is thus limited by the observation time T ($\Delta f = 1/T$) and the signal-to-noise ratio is given by:

$$\frac{S}{N} = \frac{h\sqrt{T}}{\tilde{h}_{noise}(f_0)} \tag{2.45}$$

In other words, the minimum detectable dimensionless amplitude of a periodic gravitational signal at a given frequency f_0 can be obtained by dividing the sensitivity $\tilde{h}_{noise}(f_0)$ by the square root of the integration time. This shows how periodic signals, despite their smaller amplitudes, can in principle be detected by long time observations.

2.4.1 Displacement noise

In the case of a displacement noise, $\tilde{h}_{noise}(f)$ is given by $\tilde{x}(f)/L$, where L is the arm length and $\tilde{x}(f)$ is the linear spectral density of the mirror displacement in the beam direction induced by noise.

Thermal noise is due to dissipative effects both in the suspension wires and in the mirrors.

The fluctuation-dissipation theorem states that any dissipative system is subjected to stochastic forces whose amplitudes are proportional to the square root of the temperature. Therefore, friction in wires, suspension clamps and mirrors induces stochastic forces on the mirrors and thus fluctuations of their position.

In the case of a pendulum of mass M, with a damping factor γ (defined as the friction force divided by the velocity of the mass), temperature T and resonant frequency ω_0, the linear spectral density of the stochastic force is white and it is given by [1]:

$$\tilde{F}(\Omega) = \sqrt{4k_B T\gamma}\frac{N}{\sqrt{Hz}} \tag{2.46}$$

where k_B is the Boltzmann constant. In the hypothesis of viscous damping due to collisions with gas molecules $\gamma = M/\tau$, where τ is the pendulum relaxation time. In this case the linear spectral density of the horizontal displacement of the mass X_{TN} induced by the thermal noise is

$$\tilde{X}_{TN}(\Omega) = \left(\frac{1}{(\Omega^2 - \omega_0^2) + \Omega^2/\tau^2}\right)^{1/2}\sqrt{\frac{4k_B T}{M\tau}}\frac{m}{\sqrt{Hz}}. \tag{2.47}$$

Since the pendulum frequency of the mirrors is well below the detection band (starting from few Hz), the noise has to be computed in the limit $\Omega \ll \omega_0$. In term of the dimensionless amplitude

$$\tilde{h}_{TN}(\Omega) \simeq \tilde{X}_{TN}(\Omega)/L \tag{2.48}$$

the noise in this limit is

$$\tilde{h}_{TN}(\Omega) \simeq \frac{1}{L\Omega^2}\sqrt{\frac{4k_B T\omega_0}{MQ}}\,Hz^{-1/2} \tag{2.49}$$

where Q, given by the product $\omega_0\tau$, is called *quality factor* of the suspension and is defined as the ratio of the pendulum energy dissipated in one cycle and its total energy. This means that a low dissipation suspension (i.e. high Q) reduces the thermal noise. This effect could be also obtained by increasing the mass of the mirrors, but good optical performances cannot be reached on large mirrors because of large internal stresses. The best compromise is to use quartz mirrors weighing few tens of kilograms.

Dissipation effects occur also inside the mirrors. The mirror structure can be thought as a series of high frequency harmonic oscillators each with a given frequency (ω_i), equivalent mass (M_i) and relaxation time (τ_i). At frequencies much smaller than ω_i, the linear spectral density of the mirror longitudinal displacement due to the internal thermal noise is approximately white and it is given by

$$\tilde{X}_{TN}(\Omega) \simeq \sum_i \sqrt{\frac{4k_B T}{M_i Q_i \omega_i^3}}\frac{m}{\sqrt{Hz}} \tag{2.50}$$

Thus, in order to reduce the thermal noise, mirrors with low dissipation and high frequency internal modes are desirable. The first internal mode of the Virgo quartz mirror is expected to be around 3 kHz, with a quality factor of about 106. Several damping mechanisms can affect the suspension and the internal modes of the mirror (for example internal friction of the materials, viscous damping and thermoelastic effects). The expected thermal noise in Virgo is plotted in the sensitivity curve shown in the next chapter.

Another important source of displacement noise is seismic noise [1]. The ground is permanently affected by seismic vibrations due to many factors (for example geological phenomena, tides, human activities).

The linear spectral density of the ground seismic displacement can be well approximated, between 1 Hz and several tens of Hz, by the function $10^{-7}/f^2 mHz^{-1/2}$ in all directions. The goal of the suspension system is to make the residual seismic noise at the mirror level smaller than the other noise mechanisms limiting the interferometer sensitivity (usually in this frequency range the thermal noise and the Newtonian noise described in the following). The basic idea is to suspend each mirror from a chain of pendulums. In an N-stage pendulum the horizontal motion of the suspension point, at a frequency f much higher than the normal mode ones, is transmitted to the suspended mass attenuated by a factor proportional to f^{2N}. If the resonant frequencies are below a few Hz (that means to build long pendulums) an acceptable attenuation can be achieved above 3-4 Hz. Vertical vibrations would be also partially transferred to the laser beam (horizontal) direction because of the unavoidable mechanical couplings and also because of Earth curvature, making widely separated pendulums non parallel to each other. A chain of oscillators can be realized also in the vertical direction by replacing each mass of the pendulum with mechanical filter, exhibiting the required vertical elasticity. The sophisticated mirror suspension system used in Virgo will be discussed in Chapter 3.

Another type of displacement noise is the *Newtonian noise* [11], also known as "gravity gradient noise", which is due to the Newtonian gravitation attraction of objects that are moving, resulting in a time-varying gravitational force acting on the mirror. The most important Newtonian effect is induced by seismic waves, which produce mass density fluctuations of the ground and therefore a fluctuation of the gravitational field, which couples directly to the test masses of the interferometer.

Newtonian noise, scaling with frequency as f^{-4}, is overwhelmed by seismic noise below a few Hz and by thermal noise elsewhere. It represents the ultimate limitation to the sensitivity at low frequencies, because the gravitational force cannot be screened. This means that once the minimum possible level of seismic and thermal noise is reached (which can be done by technological improvements), the Newtonian noise would be dominant, and it could not be further lowered.

2.4.2 Optical readout noise

Once any possible measure to reduce the problems due to power fluctuations of laser emission have been taken, *shot noise* is the fundamental limit for optical detection [1].

The photon shot noise in h is described by a white amplitude spectral density of magnitude

$$h_{shot}(f) = \frac{1}{L}\sqrt{\frac{\hbar c\lambda}{2\pi P_{in}}} \tag{2.51}$$

where λ is the wavelength of the laser and P_{in} is the input power.

Unfortunately, one cannot achieve an arbitrary accuracy just increasing P_{in}, as eq. (2.51) seems to suggest. In fact we have to deal with the quantistic problem of the measurement process disturbing the system under measurement. In the case of an interferometric detector, the nearly freely-falling test masses are the system to be measured, while laser, light beams and photodetector are the measuring apparatus. Fluctuating radiation pressure on the test masses cause them to move in a noisy way, and the resulting fluctuation in the length difference between the two arms can affect the phase difference between the light arriving from the two arms. The power fluctuations in the two arms will be anti-correlated, so the effect on the output of an interferometer is doubled, since the phase shift is proportional to the difference in length of the two arms. The *radiation pressure*

noise is given by:

$$h_{rp}(f) = \frac{2}{L}x(f) = \frac{1}{mf^2L}\sqrt{\frac{\hbar P_{in}}{2\pi^3 c\lambda}} \tag{2.52}$$

being $x(f)$ the spectrum of each mass motion induced by the fluctuating radiation pressure.

Thus there are two different sources of noise associated with the quantum nature of light, and they exhibit an opposite dependence on the light power: shot noise decreases as the power grows, while the radiation pressure noise increases.

These two noise sources can be treated together as a single noise called *optical readout noise*, given by the quadrature sum

$$h_{opt}(f) = \sqrt{h^2_{shot}(f) + h^2_{rp}(f)}. \tag{2.53}$$

At low frequencies, the radiation pressure term dominates, while shot noise is more important at high frequencies. The expression that optimizes the power in order to obtain the minimum noise spectral density at a given frequency f is

$$P_{opt} = \pi c\lambda m f^2. \tag{2.54}$$

Putting this expression in eq. (2.53) the lowest possible noise, i.e. the *quantum limit*, can be obtained:

$$h_{QL}(f) = \frac{1}{\pi fL}\sqrt{\frac{\hbar}{m}}. \tag{2.55}$$

h_{QL} is a "pseudo-spectral density" rather than a real spectrum, because it indicates for each frequency the minimum noise spectral density due to optical readout noise that one can obtain, having a given light power. More precisely, it is the locus of the lowest possible points of the family of spectra $h_{opt}(f)$ parametrized by f_0. It is important to stress that the maximum sensitivity achievable at a given frequency f depends only on the arm length and the mirror masses.

2.4.3 Phase noise

In addition to displacement noise and optical readout noise we have to consider phase noise [13], whose main sources are:

- *frequency instability* of the laser.

  The dephasing between the light beams depends on the laser frequency as

  $$\Delta\varphi = \frac{\omega_L}{c}\Delta L_{opt} \tag{2.56}$$

  where ΔL_{opt} is the unavoidable statical path difference between the two Fabry-Perot cavities. If ΔL_{opt} was null one could in principle obtain interference even using a white light source. Since this is not the case, any fluctuation in the laser frequency produces a dephasing of

  $$\tilde{\varphi}_\delta(f) = \frac{\tilde{\omega}_L}{c}\Delta\tilde{L} \tag{2.57}$$

  where $\tilde{\delta}(f)$ is the linear spectral density of the frequency fluctuations.

  The slight differences between the reflectivity of the mirrors produce differences in the finesse of the cavities, inducing asymmetry in the optical path $\Delta L_{opt}/L_{opt} \simeq 1\%$. In these conditions, a fluctuation of the wavelength $\tilde{\delta}(f) = 10^{-5} Hz/\sqrt{Hz}$ is allowed. The laser frequency fluctuation is in general much higher, and a frequency stabilization system is thus necessary.

- *Air density fluctuations* in the two arms introduce random variations in the refraction index, and thus in the light optical path difference. The whole apparatus needs to be in vacuum to suppress this noise. In typical interferometer antennas a residual pressure of 10^{-6} mbar is achieved. This keeps the residual phase error well below the shot noise in all the detection band [13].

- *Light scattered* from residual air can re-enter the beam by reflection from the tube walls. Part of the small amount of light scattered off by the mirrors can recombine with the main beam by a further mirror scattering, after having interacted with the cylindrical vacuum pipe walls. This spurious light follows a different optical path modulated by the pipe seismic vibrations. A phase noise is thus induced in the interference signal. For this reason absorbing baffles are assembled inside the kilometer-scale vacuum pipes in order to absorb the diffused light and make this noise well below the antenna sensitivity [14], [15].

- *Laser power fluctuations* inside the interferometer can be converted to phase noise. Also in this case, the asymmetry between the two cavities sets the requirements for the laser power stabilization. The power fluctuations of the type of laser used in the interferometric detectors are larger at low frequency; in Virgo, it is therefore necessary to modulate the laser (at 12 MHz) to shift the detection signal to a lower noise spectral region [16].

- *The presence in the beam of different propagation modes* makes it impossible to fix the same condition of resonance for all the photons in the beam. To solve this problem gravitational wave interferometers use a system called *mode cleaner* that sharpens the beam before it enters the interferometer, selecting the main Gaussian mode (TEM_{00}). The mode cleaner is a suspended cavity with a very high finesse, and its shape is triangular in order to avoid reflections back towards the laser.

Chapter 3

Virgo interferometer

The gravitational wave detector *Virgo*, funded by CNRS (France) and INFN (Italy), is a recycled Michelson interferometer where each arm is replaced by a 3 km long Fabry-Perot cavity. Virgo is located at the European Gravitational Observatory (EGO), close to Cascina (Pisa, Italy), and is designed to detect gravitational waves emitted by astrophysical sources in the frequency range between a few Hz and a few kHz. Recently other groups from the Netherlands, Poland and Hungary entered the joint effort. Virgo is the unique detector that, from the beginning, thanks to its special anti-seismic isolation system, extended the detection band down to about 10 Hz.

As shown in the picture in Fig.(3.1) there are several buildings in the detector site: all the optics of the interferometer, including the two Fabry-Perot input mirrors, are located in the central building. In the terminal buildings (3 km far from the central one) the Fabry-Perot end mirrors are located. All the operations of the instrument are performed remotely by the control room located in the building visible closest to the road.

Each of the six main optical components (recycling mirror, beam-splitter and Fabry-Perot cavity mirrors) is suspended from a 8 m long *Superattenuator*, the special attenuation system used to filter the seismic vibrations. Smaller anti-seismic suspensions are used to isolate the optical benches and

Figure 3.1: *Aerial view of Virgo interferometer in Cascina (Pisa).*

the input *mode cleaner* mirror described in the following. This last mirror is placed at the end of a triangular cavity about 144 m long (and located in the small additional building, visible on the left of the central one). The entire system is in a high vacuum environment. In particular the Fabry-Perot cavities are contained in 3 km long pipes with a diameter of 1.2 m, located in the long tunnels appearing in the picture.

3.1 The optical scheme

The whole source apparatus consists of three benches [17]: two optical tables (the *laser bench* and the *external injection bench*), ground connected, seismically isolated by pneumatic legs, installed within a clean-room laboratory with controlled temperature, and the *suspended injection bench*, hung to a two stage multi-pendulum, in a vacuum bell at 10^{-6} mbar separated from the laboratory environment by an optical window [18].

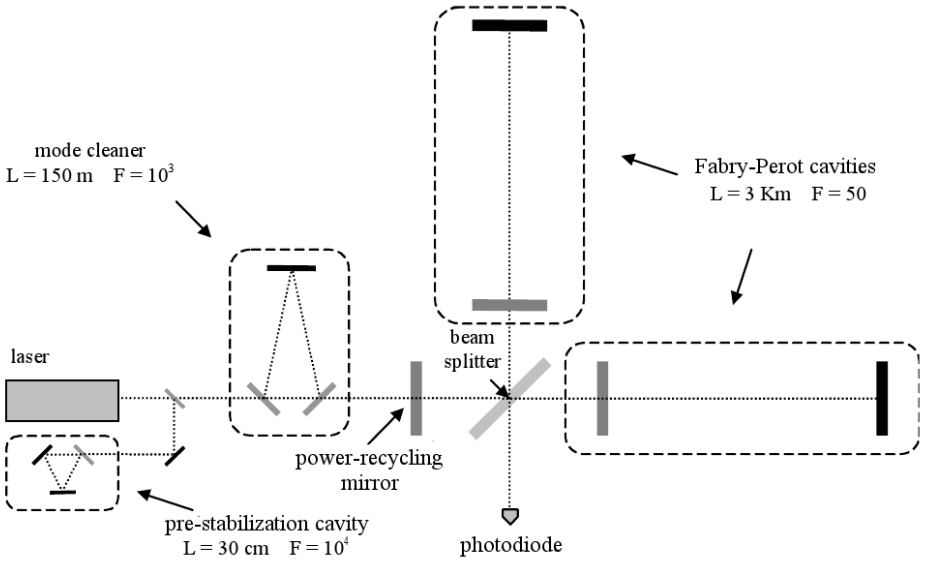

Figure 3.2: *Schematic representation of Virgo [13]*

The laser bench contains the laser, the optical isolators and two phase modulators. The light beam is generated by a 20 W high-power Nd:YVO4 laser source locked to a 1 W solid state Nd:Yag master laser, and is then sent to the external injection bench, to be correctly aligned with respect to the detector reference frame before entering the vacuum system. The amplitude stabilization is performed by taking part of the light at the laser output from one of the plane mirrors of the cavity, and then acting on the current of the slave laser diodes. After the slave laser there is the electro-optic modulator for the stabilization of the reference cavity and then two Faraday isolators that reject the back-reflected light. On the external injection bench there are all the detectors for the stabilization of various parameters (frequency, amplitude and beam geometry) matching with the reference cavity and with the following mode cleaner. The beam entering the suspended injection bench is focused by a telescope on the input mode cleaner. The latter consists in a triangular cavity 144 m long, with two flat mirrors optically connected to a dihedron and a curved one, suspended from a short suspension chain.

The purpose of the input mode cleaner is to spatially filter the beam, selecting a TEM_{00} mode, before the interferometer input, and to stabilize the laser frequency. In the low frequency region (below 15 Hz) the input mode cleaner is stabilized by using a 30 cm long rigid reference cavity hung under the suspended injection bench.

After the mode cleaner, a telescope focuses the beam into the interferometer. This starts with a beam-splitter with reflectivity $r = 0.5$, inclined by 45° with respect to the beam direction. The beam-splitter separates the beam in two equal and coherent parts, which propagate into the two arms of the interferometer, each constituted by a Fabry-Perot cavity. The distance between the mirrors, installed within vacuum towers at each end of the cavities, is $L = 3$ km. In both arms the first mirror is flat and it has reflectivity $r_1 = 0.88$, i.e. a part of the beam is transmitted and recombined with the light reflected at the first impact, while the second mirror is curved, with curvature radius $r_{curv} = 3450$ m, and it is totally reflecting ($r = 0.9999$). As shown in sec. (2.3.1), the light beam performs many bounces inside the cavity before exiting it. The effective path length in Virgo arms is about 100 km. The Gaussian beam has a radius on the flat mirror of ~ 54.9 mm, with a Rayleigh range of ~ 1161.06 m.

The exact position of the beam-splitter with respect to the input mirrors of the Fabry-Perot cavities is determined in order to keep the interferometer output carrier in the dark fringe, while the sidebands are transmitted. We have constructive interference on the sidebands for

$$\frac{\omega_0 + \Omega}{c} 2L_x - \frac{\omega_0 + \Omega}{c} 2L_y - \pi = 2\pi n$$
$$\Rightarrow L_y - L_x = \Delta L = \frac{c}{\Omega}\frac{\pi}{2} = \frac{\lambda_{mod}}{4}, \quad (3.1)$$

where Ω is the modulation frequency and $\omega_0 + \Omega$ is the frequency of the upper sideband [17].

The interferometer works at the dark fringe, and the beam, apart from

losses, is fully recombined in the direction of the source. In such condition, it is possible to recycle the light with the *power-recycling* technique [19]. A mirror with high reflectivity ($r_{rec} = 0.95$), called *power-recycling mirror*, is located before the beam-splitter. This creates another Fabry-Perot cavity between itself and the full interferometer that can be thought of as a mirror reflects the light towards the source. The beam power hitting the beam-splitter is amplified this way and the shot noise reduced. The power-recycling mirror M_R is a convex mirror that works as a lens, with curvature radius $r_{R,curv} \sim 4$ m. The coating is on the plane surface towards the interferometer. The power is amplified by a recycling factor of about 35. The distance between the power-recycling mirror and the beam-splitter is 6 m. The presence of the power-recycling modifies the optimal asymmetry, because the length ΔL that would maximize the sideband transmission without power-recycling is not necessarily the one that maximizes the storage in the power-recycling cavity, which is also a function of asymmetry. The maximum sideband transmission occurs for

$$\cos\left(\frac{\Omega \Delta L}{c}\right) = r_{rec} r_{ITF}(\omega_0 \pm \Omega) \tag{3.2}$$

where $r_{ITF}(\omega_0 \pm \Omega)$ is the one of the interferometer at $\omega_0 \pm \Omega$ [17].

In the interferometer output there is a main beam reflected by the beam-splitter reflecting surface on the dark fringe, and a secondary beam coming from the reflection on the other surface of the beam-splitter. The gravitational wave signal is in the main beam, but both the beams are used for checking the interferometer position.

This detection system consists in a *suspended detection bench* maintained in vacuum, and in an optical table located outside the vacuum tower, the *external detection bench*. The former, attached to a superattenuator, focuses both the beams and cleans the main beam, while on the latter there are the InGaAs photodiodes for the signal detection and for the interferometer lock-

ing [18]. We remind that the relative position of the suspended mirrors has to be fixed with high accuracy (picometers) to keep the cavity at resonance and the interferometer on the dark fringe. This control, involving four longitudinal degrees of freedom, is made by using additional photodiodes at the output ports of the interferometer. They produce the error signals and the mirror position is corrected by coils acting on magnets glued on the back of the mirror [20]. This system filters the dark fringe, detects the gravitational wave signal and partially produces the locking signals to the interferometer. Since there are many imperfections such as optical defects or asymmetries that could produce higher modes in transmission, there is an *output mode cleaner* on the suspended detection bench. This mode cleaner is a monolithic cavity of 25 mm, curvature radius 3 m and finesse 50 [17]. It filters all the higher order optical modes of the main beam.

The main beam, separated from the secondary one and focused, passes through the mode cleaner. A fraction of this transmission is taken and is sent to a photodiode on the external bench for the interferometer locking, and to monitoring cameras. The gravitational signal is in the beat between the carrier and the transmitted sidebands. The secondary transmission of the interferometer is partly (90%) sent to a photodiode on the external bench for the interferometer locking, while the remaining 10% is sent to sensors on the suspended detection bench for its stabilization. Once the interferometer is locked, the automatic alignment system is switched on. Photodiodes are used to align the mirrors with an accuracy of fractions of nanoradians [21]. This allows to increase the contrast at the output phase and the sensitivity of the apparatus.

3.2 Seismic noise attenuation

As we already saw in sec. (2.4.1), seismic noise is dominating at low frequencies. In order to reduce seismic noise transferred to the mirrors, the

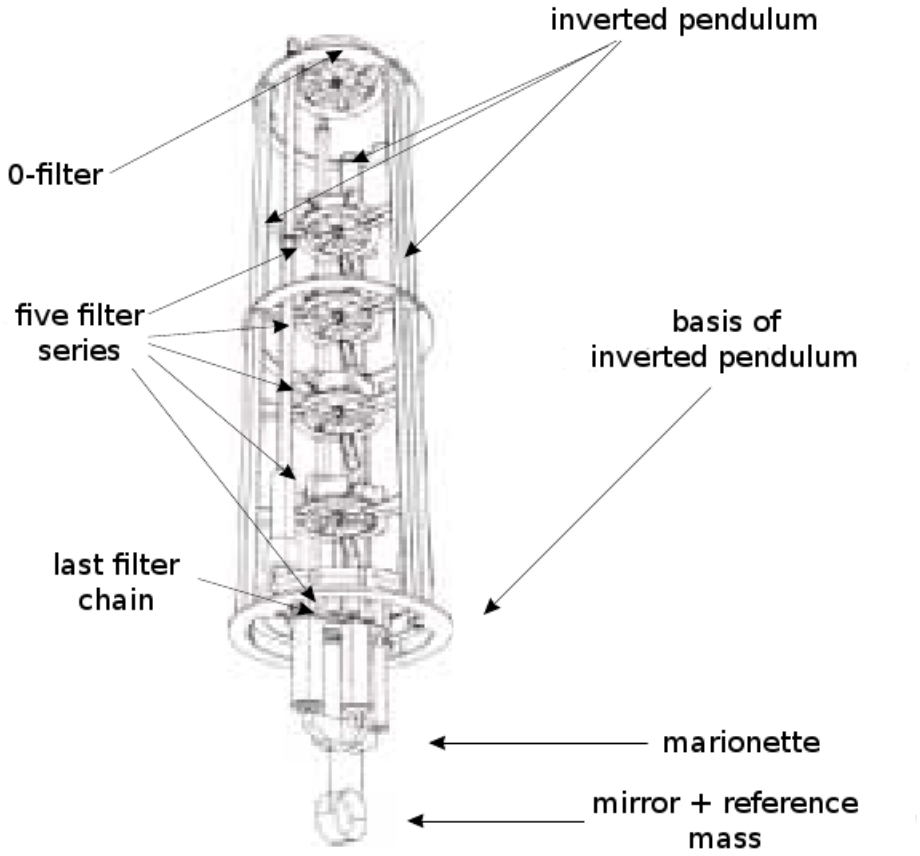

Figure 3.3: *Virgo superattenuator scheme [12].*

Virgo collaboration has developed a particular system of suspensions called *superattenuator* (SA, Fig. (3.3)) [22].

The SA (Fig. (3.3)) is essentially a five stage pendulum. In an N-stage pendulum the horizontal motion of the suspension point, at a frequency f much higher than the normal mode ones, is transmitted to the suspended mass attenuated by a factor proportional to f^{2N}. The Superattenuator chain is long enough (about 8 m) to confine all its normal modes below 2.5 Hz. In this way a remarkable attenuation of the horizontal groun seismic noise can be achieved starting from a few Hz. Vertical mirror vibrations are also partially transferred to the laser beam (horizontal) direction because

of unavoidable mechanical couplings[1] (estimated to be well below 1%). Another oscillator chain can be realized in vertical to filter seismic vibrations also along this direction. Each mass of the pendulum chain was replaced by a special mechanical filter, exhibiting the required vertical elasticity (see [23] and its references). Also the rotational modes of the chain about the vertical axis are all below 1 Hz thanks to the large inertial momentum of the filters and the small suspension wire thickness. The tilt of the ground is also strongly suppressed along the chain. From the last filter of the chain it is suspended the *Optical Payload*, a system composed by three items: *Marionette*, the mirror and its *Reference Mass* [24]. The Marionette (see Fig. (3.3)) is steered by four coils each placed at the end of a 1 m long cylinder extending from the last stage of the SA and acting on a permanent magnet mounted on the Marionette arms. The mirror and its reference mass are suspended in parallel from the Marionette each by a cradle formed by a couple of 1.9 m long thin wires. The mirror position can be controlled in three degrees of freedom (the longitudinal displacement along the beam and the rotation about the other two axes) both by Marionette coil-magnet actuators and by four coils located on the Reference Mass, each acting on a magnet glued on the back of the mirror.

In the resonance range, well below the detection band frequency threshold, the chain horizontal resonances excited by seismic noise make the mirror widely swinging (several microns along the beam direction). This displacement has to be compensated at the level of the optical payload to maintain the mirrors in the longitudinal working position with a very large accuracy (of the order of picometers). On the other hand too large compensation forces close to the mirror are not acceptable. Indeed the electro-mechanical

[1] The Earth curvature makes widely separated pendulums non parallel to each other with about 3.10^{-4} rad plumb line misalignment on a 3 km scale. As a consequence, even assuming a null mechanical coupling, a vertical-horizontal transmission of this entity takes place.

actuation system induces a white noise force (affecting the entire Virgo band) proportional to the maximum required compensation amplitude. With the present electronics dynamics, the maximum horizontal displacement that can be adjusted acting by the payload actuators without affecting the antenna sensitivity is a few tenths of micron. A preliminary reduction of the tens of microns mirror swing induced by mechanical resonances is thus necessary.

For this reason the top stage of the chain, formed by another mechanical filter named *Filter Zero*, is suspended by three thin wires from a three legs elastic structure called *Inverted Pendulum* [23]. The elasticity is given by a flexural joint on which each leg is based. By keeping the horizontal resonant frequency of the inverted pendulum at 30-40 mHz a significant attenuation in the horizontal direction is achieved also in the pendulum chain resonance range (from 100 mHz to 2 Hz).

An active inertial system acting on the suspension top stage (*Inertial Damping*, see [25]), is used to further decrease the mirror swing to be compensated acting on the optical payload down to an acceptable level. Three high sensitivity accelerometers [22] were developed and assembled on the Inverted Pendulum top stage to monitor with high accuracy its acceleration in the horizontal plane (two translations and one rotation about the vertical axis). Three coil-magnet actuators are then used in feed-back to keep the position of the Inverted Pendulum top stage locked to the inertial system. An effective active damping of the suspension resonances were obtained in this way. A similar system was assembled on the vertical degree of freedom, where accelerometers and coil-magnet actuators were used on the filter zero movable part.

In order to reduce as much as possible the compensation force at the mirror level a hierarchical control strategy was adopted in the SA (see [26] for details). The hundreds of microns large seismic motion taking place in

the ultralow frequency range (below 10 mHz) because of tides and drift was controlled by the top-stage using the interferometer signal as a sensor. The wide electronic floor induced by this large actuation force is suppressed by the filter chain below. The residual optical payload displacements (up to a fraction of microns) are compensated between a few tens of mHz and a few Hz at the level of the marionetta with the electromechanical floor attenuated by the mirror pendulum. Only small compensations (above a few Hz) are compensated acting directly at the mirror level. The measured actuation noise floor in the detection band was measured not to affect the Virgo sensitivity and also the new generation interferometer (*Advanced Virgo*).

3.3 Virgo sensitivity

The minimal amplitude of the gravitational wave detectable by the instrument depends on its *strain sensitivity* $\tilde{h}_n(f)$. The total noise spectral density is defined as the superposition of the spectral power of each noise source [13].

- *Seismic noise* is dominant at low frequencies, below the superattenuator resonances (0.03 - 2.5 Hz). It becomes rapidly negligible for higher frequencies, due to the strong filtering, scaling as a high power of the frequency (f^{-16}). At a frequency of about 3 Hz the crossing with thermal noise and Newtonian noise is expected ($\tilde{h}_{seis} \simeq \tilde{h}_{therm} \simeq \tilde{h}_{newt} \simeq 5 \cdot 10^{-20} \cdot 1/\sqrt{Hz}$). Seismic noise amplitude increases again over 10 Hz because of structural resonances of parts of the attenuator, but its spectral density is well below the shot noise.

- *Thermal noise* is the main noise source between 3 Hz and 150 Hz. It is of the same order of shot noise between 150 Hz and 400 Hz ($\tilde{h}_{therm} \simeq \tilde{h}_{shot} \simeq 2 \cdot 10^{-23} \cdot 1/\sqrt{Hz}$). In the first part of the spectrum the dominant contribution to thermal noise is given by mirror suspension wires, and it goes as $f^{-\frac{5}{2}}$. Over about 50 Hz it is more important the

contribution of mirror thermal fluctuations, that scales with frequency as $f^{-\frac{1}{2}}$. At every frequency multiple of a frequency between 100 and 200 Hz there are very narrow and high noise peaks which correspond to the suspended wires violin modes. A higher peak due to the first internal resonance of the mirror is visible at about 5 Hz.

- *Newtonian noise* is less important than seismic noise below 3 Hz, and is dominated by thermal noise above this frequency, because it decreases with frequency as f^{-4}. This noise is relevant on the detector sensitivity only near the lower limit of the detection band, where it is comparable with the other two.

- *Shot noise* is dominant at high frequencies, except for the exact frequencies where there are the thermal noise peaks previously described. Though its frequency independence, it shows a slight tendency to become stronger above 500 Hz. This effect is due to the detector loss of sensitivity in the region where photon flight time becomes comparable to the gravitational wave period. At 10 kHz the spectral density grows of over an order of magnitude ($\tilde{h}_{shot} \simeq 4 \cdot 10^{-22} \cdot 1/\sqrt{Hz}$).

In Fig. (3.4) the linear spectral densities corresponding to the dominant noise mechanisms is plotted.

3.4 The first Virgo Scientific Run

The first Virgo Science Run (VSR1) started on May 18, 2007 in coincidence with the last period of the LIGO S5 run. Even if the detector sensitivity was noisier than expected all over the bandwidth, in the frequency region 300 Hz-5 kHz the design sensitivity has been reached and it is comparable to the LIGO one (see Fig. (3.5)). This result has been considered appropriate to start joint data analysis with the LIGO Scientific Collaboration (LSC). The VSR1 has been stopped on October 1st, 2007 (in coincidence with the

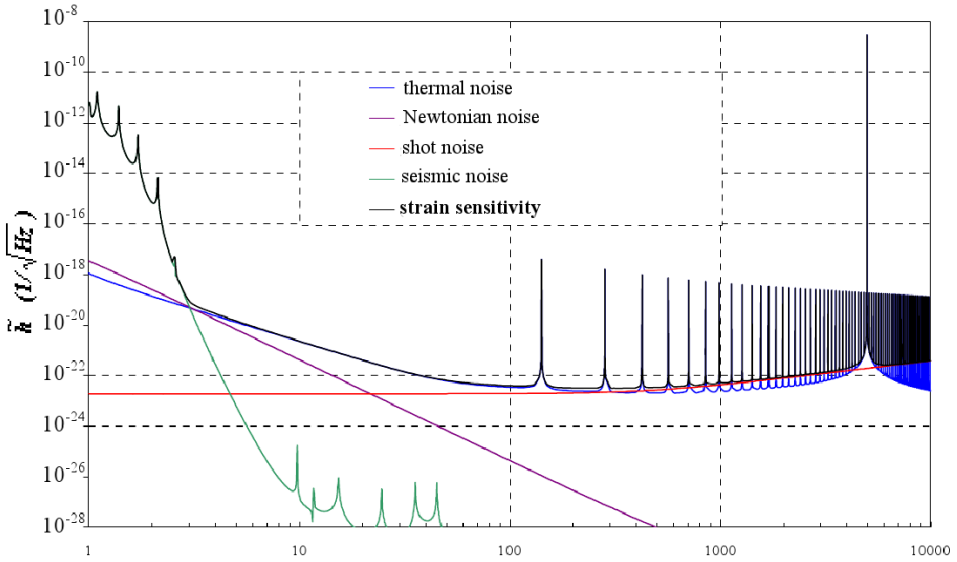

Figure 3.4: *Spectral density of main Virgo noises, expressed by equivalent field [13]*

end of S5) after about four months of continuous data taking. The detector duty-cycle in science mode has been as high as 81% with about 20 sets of un-interrupted data collection longer than 40 hours very promising for future data analysis. These good results have been obtained thanks to the locking automation procedure and to the fine tuning of the complex feedback control systems. Even if the design sensitivity is not yet reached all over the bandwidth, the Virgo interferometer shows the best sensitivity in the world in the frequency range below 35 Hz [18]. Up to now, no evidence of gravitational wave signals was found in VSR1 data.

3.5 Virgo upgrades

On July, 7^{th} 2009, after a couple of years of commissioning and upgrading, the new Scientific Run started (VSR2). The present sensitivity, as shown in Fig. (3.6), is very close to the design one even in the low frequency range. The upgrading of the experiment (*Advanced Virgo*) is foreseen in the next

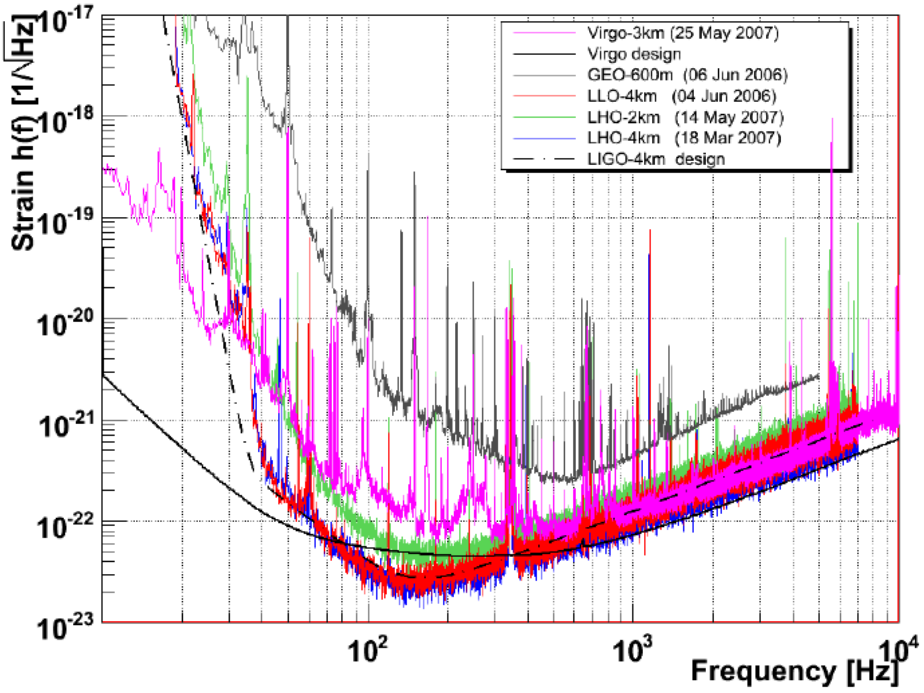

Figure 3.5: *Sensitivity curves comparison for different detectors (Virgo, LIGO and GEO-600 m) [18].*

years. The goal is to increase the detector sensitivity in the whole band by about a factor 10 with respect to the present one. Advanced Virgo, which is expected to run in coincidence with the parallel American upgraded project (*Advanced LIGO*), is starting from 2014.

3.6 Other gravitational wave antennas

In addition to the already mentioned U.S.A. LIGO project [28], other interferometers, based on the same principle, are in action all around the world. They are the 300 m Japanese interferometer TAMA close to Tokyo [29] and the British-German antenna 600 m long arm antenna GEO close to Hannover [30]. Other projects for the development of a second generation interferometers are under approval in Japan (LCGT [31]) and in Australia

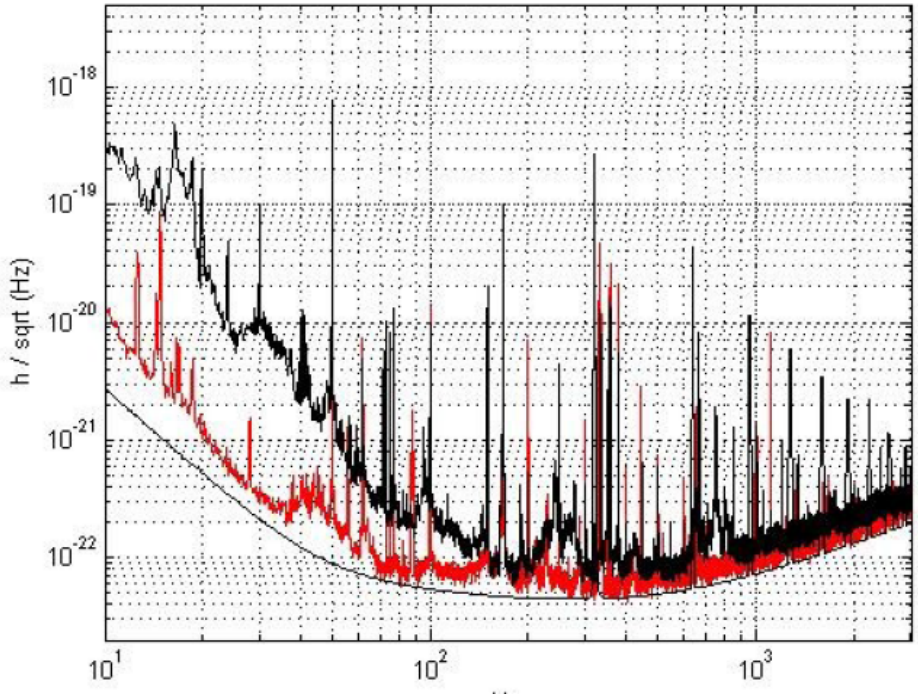

Figure 3.6: *Current sensitivity curve (red plot), compared to the VSR1 sensitivity (black plot) and to the design sensitivity (grey plot) [27].*

(AIGO [32]).

Not every gravitational wave detectors are interferometers. The first gravitational wave detectors have been developed during the 1960s by Joseph Weber [33]. He proposed to measure the stress engendered by the gravitational wave on a suspended resonating bar. Since the particles are connected by elastic forces, a bar is expected to oscillate after the excitation produced by the gravitational wave. A bar detector is a suspended Given the small detection band and the low sensitivity with respect to interferometric antennas, developments of bar detectors has been stopped. At the present time only three bar antennas are running (AURIGA, NAUTILUS and EXPLORER, see bar network website [34] and its links). The comparison between broadband interferometer data and narrow band bar data is in fact

appropriate particularly in burst and stochastic background searches [35]. Furthermore, bar detectors provide detection continuity during the periods in which interferometers are not running.

Chapter 4

Detection of Continuous Waves

A periodic source emits gravitational waves continuously mainly at the double of its rotational frequency. Since the emission is directly related to the intrinsic rotational behavior of the star and not to occasional events such as for coalescing binaries or Supernovae explosions, a signal belonging to this particular class will always be present in any data stream. As we already mentioned in sec. (1.5.3), the longer is the observation time, the larger is the probability of detecting a gravitational wave emitted by a rotating Neutron Star. This is true because the signal-to-noise ratio, for a signal at fixed frequency, goes as the square root of the integration time [11]. In fact, if a signal $h(t)$ with a known form is buried into a noise $n(t)$ higher than $h(t)$, we can multiply the output $s(t) = h(t) + n(t)$ by $h(t)$, integrate over the observation time T and then divide by T, obtaining

$$\frac{1}{T}\int_0^T dt\ s(t)h(t) = \frac{1}{T}\int_0^T dt\ h^2(t) + \frac{1}{T}\int_0^T dt\ n(t)h(t). \qquad (4.1)$$

Since the first integrand on the right-hand side is definite positive, this integral grows as T; its value averaged over a time T is $\sim h_0^2$, being h_0 the

characteristic amplitude of the oscillating function $h(t)$. On the contrary, the second integrand is oscillating, since $n(t)$ and $h(t)$ are uncorrelated. Its integral is a stochastic variable that can be either positive or negative, and its *rms* will then grow only as $T^{1/2}$:

$$\frac{1}{T}\int_0^T dt\; n(t)h(t) \sim \left(\frac{\tau_0}{T}\right)^{1/2} n_0 h_0, \tag{4.2}$$

where n_0 is the characteristic amplitude of the oscillating function $n(t)$ and τ_0 is the period of $h(t)$. The latter term then averages to zero when $T \to \infty$. Thus, to distinguish the signal $h(t)$ from the noise we should choose T in such a way that $h_0 > \left(\frac{\tau_0}{T}\right)^{1/2} n_0$.

The expression of the signal produced in the detector by a source emitting gravitational waves has already been expressed in eq. (2.24) using the pattern functions $F_+(\theta, \phi)$ and $F_\times(\theta, \phi)$.

Even assuming the source perfectly periodic, the signal received by an interferometer on Earth would be very different from the one described by eqs. (2.24)-(2.26), because the motion of the Earth introduces several effects that modulate the signal and make it different from its original shape. The Earth motion with respect to the Solar System Barycenter (SSB) induces a variation in time of the relative velocity Earth-source, and this produces a time-varying Doppler-shift in the frequency. Besides, the Earth rotation makes the apparent position of the source changing, so the angles θ and ϕ are not constant, but change periodically with the sidereal time. The dependence of pattern functions on $\theta(t)$ and $\phi(t)$ introduces thus an amplitude modulation in the detected signal.

4.1 Doppler shift and phase modulation

The Doppler effect due to the Earth motion with respect to the SSB introduces thus a *frequency modulation* in the observed signal [1]. The frequency

of the received wave is

$$f = f_0 \left(1 + \frac{\vec{v} \cdot \hat{r}}{c}\right), \tag{4.3}$$

where f_0 is the frequency of the original monochromatic signal, $\vec{v}$ is the velocity of the antenna with respect to the source, and $\hat{r}$ is the source direction. Since $\vec{v} \cdot \hat{r}$ is a function of time, this introduces the time-dependence in the observed frequency. We can give an estimate of how much important this effect is by separately computing it for the Earth rotation around its axis and for its orbital motion around the Sun [11].

Denoting by $(\Delta v)_T$ the change of the component of the velocity in the direction of the source in a time T, then the change in frequency during the same time is

$$(\Delta f)_{Doppler} = f_0 \frac{(\Delta v)_T}{c}. \tag{4.4}$$

The Doppler effect can be neglected as long as $(\Delta f)_{Doppler}$ is smaller than the frequency resolution $\Delta f = 1/T$. In the approximation of a circular orbit $(\Delta v)_T \sim v_{rot}\omega_{rot}T$, where v_{rot} and ω_{rot} are the rotational velocity of the Earth and its rotation frequency, one obtains that $(\Delta f)_{Doppler}$ becomes of the order of the frequency resolution for

$$f_0 \left(\frac{v_{rot}}{c}\right) \omega_{rot} T \sim \frac{1}{T}. \tag{4.5}$$

Therefore the integration time over which the Doppler effect is still negligible is

$$T \sim 60\ min\ \left(\frac{1\ kHz}{f_0}\right)^{1/2}. \tag{4.6}$$

The maximum frequency shift induced by the rotation of Earth around its axis is

$$(\Delta f)^{max}_{rot} \sim 2 f_0 \frac{v_{rot}}{c} \simeq 2.4 \cdot 10^{-3}\ Hz\ \left(\frac{f_0}{1\ kHz}\right). \tag{4.7}$$

The same argument is true for the Earth revolution around the Sun. In this case, the maximum frequency shift is

$$(\Delta f)^{max}_{orb} \sim 2 f_0 \frac{v_{orb}}{c} \simeq 0.2\ Hz\ \left(\frac{f_0}{1\ kHz}\right) \tag{4.8}$$

where a circular orbit was considered [11]. $(\Delta f)_{orb}^{max}$ is much larger than $(\Delta f)_{rot}^{max}$, since $v_{orb} \gg v_{rot}$. The time after which the orbital Doppler shift becomes larger than the frequency resolution is:

$$T \sim 120\ min\ \left(\frac{1\ kHz}{f_0}\right)^{1/2}. \tag{4.9}$$

The effect due to the Earth rotation is thus the first to become relevant when the integration time in eq. (4.6) increases, but the orbital Doppler shift raises steadily with T, and it takes less than one day to become the dominant effect.

The detection of the small signals emitted by Pulsar requires very long integration time ($T \simeq 10^7\ s$) to distinguish the spectral peak from the noise floor. It is clear that the effect of Doppler shift in the signal received by the detector has to be corrected. Let us consider the simple case of a detector moving with constant velocity, along a circular orbit around the Sun and pointing to the source with fixed orientation. According to [36] the detected signal will be

$$A(t) = A_0 \cos\left(\omega_0 t + \varphi(t)\right) \tag{4.10}$$

where $\varphi(t) = \varepsilon \sin(2\pi f_y t)$. f_y denotes the orbital frequency while ε is the amplitude of the phase variation due to the Doppler effect. This is called *phase modulation index*, defined as

$$\varepsilon = \frac{f_0}{f_y}\frac{v}{c} = \frac{2\pi r}{\lambda}. \tag{4.11}$$

For the rotation of the Earth around its axis $\varepsilon \simeq 100(f_0/1\ \text{kHz})$, while for the orbital motion $\varepsilon \simeq 3 \cdot 10^6 (f_0/1\ \text{kHz})$ [11]. The frequency modulation is thus

$$\Delta f = f - f_0 = \varepsilon f_y \cos(2\pi f_y t). \tag{4.12}$$

Eq. (4.10) can be expressed as a superposition of monochromatic waves using the identity

$$A_0 \cos\left(\omega_0 t + \varepsilon \sin(\omega_y t)\right) = A_0 \sum_{-\infty}^{+\infty} J_n(\varepsilon) \cos(\omega_0 + n\omega_y)t \tag{4.13}$$

where $J_n(\varepsilon)$ are the Bessel functions of the first kind. The signal is therefore split into a carrier at the frequency f_0, plus an infinite number of sidebands at $f_0 \pm n f_m$, for n any integer. The signal energy is not affected by the phase modulation but it is spread on a band Δf whose halfwidth is given by the frequency modulation amplitude, εf_y, and the power in the n^{th} sideband is proportional to $J_n^2(\varepsilon)$. Reducing the modulation index has then the effect of reducing the width of the band over which the energy is spread. For $\varepsilon = 1\ rad$ we would have $J_0 = 0.765198$, so the carrier would keep more than 75% of the signal amplitude (about 60% of the energy).

We can now define a new variable $t' = t + \frac{\vec{x}(t)\cdot\hat{r}}{c}$, where $\vec{x}(t)$ is the position of the detector expressed in the reference frame of the SSB, and $\hat{r}$ is the direction of the source. Introducing t' in eq. (4.10), the signal is simply proportional to $\cos(\omega_0 t')$, and in its Fourier transform all the sidebands produced by the Doppler effect collapse into a single frequency. Therefore a simple method to correct the Doppler shift consists in resampling the output of the detector in terms of t'. This causes also the broadening of monochromatic lines due to instrumental noise and helps us to discriminate a real gravitational wave signal from the noise.

Both $\vec{x}(t)$ and $\hat{r}$ have to be known with a large accuracy. The motion of the Earth, and thus the antenna one, is precisely known from the ephemeris given by the NOVA satellite [37]. We have to estimate the accuracy on sky direction needed to correct the Doppler shift. From eq. (4.3) one can infer the angular resolution in rads of the source position so to have a peak recovery within the frequency resolution $1/T$. In other words, one can write:

$$\frac{f_0}{c}\,(\Delta v)_T\,\Delta\theta < \frac{1}{T} \tag{4.14}$$

where $\Delta\theta$ is the angular resolution in radians on the position of the source. Assuming that the Doppler effect due to the orbital motion dominates the one due to Earth rotation around its axis, we can consider $(\Delta v)_T \sim v_{orb}\omega_{orb}T$.

The accuracy needed for the source direction is thus:

$$\Delta\theta < \frac{1}{f_0(v_{orb}/c)\omega_{orb}T^2} \simeq 0.1 arcsec \left(\frac{10^7 s}{T}\right)\left(\frac{1\ kHz}{f_0}\right). \tag{4.15}$$

This requirement is easily satisfied for targeted searches, i.e. in case the position of the source is measured by its electromagnetic emission. It is very interesting, though, to perform *blind searches*, sweeping the whole sky looking for unknown sources. The celestial sphere should be divided in cells with a size given by eq. (4.15) and apply a Doppler correction for each of them. The correction should be provided for more than 10^{11} seconds to detect 100 Hz signals, that is prohibitive from computational point of view.

We have assumed in the previous argument that the intrinsic frequency f_0 of the source is stable within the resolution $\Delta f = 1/T$. The electromagnetic and gravitational radiations, however, induce energy losses, which is taken from the rotational energy of the pulsar. The evolution of the pulsar frequency can be expressed as a Taylor expansion around some reference value of the pulsar proper time $T_0 = 0$:

$$f(T) = f_0 + \dot{f}_0 T + \frac{1}{2}\ddot{f}_0 T^2 + ... \tag{4.16}$$

It is thus necessary to take into account at least the first order of the *spin-down parameters* to correct the Doppler phase modulation. This parameter can be measured for known pulsars, but introduces another unknown quantity for blind searches.

4.2 Amplitude modulation

As shown in sec. (2.2), the Earth rotation around its axis affects also the pattern functions, which are periodic functions of sidereal time. This introduces an *amplitude modulation* in the signal received by the detector. To consider this further modulation in the correction of the detector output, the time dependence of the pattern functions F_+ and $F_\times$ introduced in eq.

(2.24) can be expressed as follows:

$$F_+(t) = \sin\zeta\,[a(t)\cos 2\psi + b(t)\sin 2\psi] \tag{4.17}$$

$$F_\times(t) = \sin\zeta\,[b(t)\cos 2\psi - a(t)\sin 2\psi] \tag{4.18}$$

where ψ is the polarization angle while $a(t)$ and $b(t)$ are known functions of many fixed quantities [38]: right ascension α and declination δ of the source, the angles λ, γ and ζ which determine the position and geometric characteristics of the detector, the angular velocity of the Earth Ω_r and the characteristic phase ϕ_r, which defines the position of the Earth in its diurnal motion at $t = 0$. Therefore the beam-pattern functions can be computed at any time for any detector.

The phase of the gravitational wave can be written as

$$\Psi(t) = \Phi_0 + \Phi(t) \tag{4.19}$$

where $\Phi(t)$ is the frequency Taylor expansion [38]:

$$\Phi(t) = 2\pi \sum_{k=0}^{s} f_0^{(k)} \frac{t^{k+1}}{(k+1)} + \frac{2\pi}{c}\hat{n}_0 \cdot \vec{r}_d(t) \sum_{k=0}^{s} f_0^{(k)} \frac{t^k}{k+1}, \tag{4.20}$$

where $f_0^{(k)}$ is the k^{th} time derivative of the instantaneous frequency evaluated at $t = 0$ at the SSB, $\hat{n}_0$ is the constant unit vector in the direction of the star in the SSB reference frame and $\vec{r}_d$ is the position vector of the detector in that frame. The gravitational wave signal can be written as

$$h(t) = h_+(t) + h_\times(t) \tag{4.21}$$

where $h_+(t)$ and $h_\times(t)$ are the polarization components of the signal:

$$h_+(t) = \frac{1}{8}h_0 \sin 2\theta \sin 2\iota \cos\Psi(t) + \frac{1}{2}h_0 \sin^2\theta(1+\cos^2\iota)\cos 2\Psi(t) \tag{4.22}$$

$$h_\times(t) = \frac{1}{4}h_0 \sin 2\theta \sin\iota \sin\Psi(t) + h_0 \sin^2\theta \cos\iota \sin 2\Psi(t), \tag{4.23}$$

where the *wobble angle* θ is the angle between the total angular momentum vector of the star and its axis of symmetry and ι is the angle between the

total angular momentum vector of the star and the direction from the star to the Earth. We will consider $\theta \simeq \pi/2$, that means that the star is rotating along the antenna orbital plane. In this case the term ruling the emission at the rotational frequency in both eqs. (4.22) and (4.23) vanishes. The amplitude h_0 is given by

$$h_0 = \frac{16\pi^2 G}{c^4}\frac{\epsilon I f^2}{r}. \tag{4.24}$$

where f is the sum of the star rotation frequency and the frequency of precession, I is the moment of inertia with respect to the rotation axis, r is the distance from the star and ϵ is the poloidal ellipticity of the star, defined as

$$\epsilon = \frac{I_1 - I_2}{I}. \tag{4.25}$$

I_1 and I_2 denote the star moments of inertia with respect to the principal axes orthogonal to the rotation axis. Taking into account eqs. (4.17) and (4.18) the signal in (4.21), detected by the antenna as $\Delta L/L$ (see sec. (2.1)) is:

$$h(t) = \sum_{i=1}^{4} A_i h_i(t) \tag{4.26}$$

where the constant amplitudes A_i depend on the parameters h_0, θ, ψ, ι and Φ_0 as follows:

$$A_1 = h_0 \sin\zeta \sin^2\theta \left[\frac{1}{2}(1+\cos^2\iota)\cos 2\psi \cos 2\Phi_0 - \cos\iota \sin 2\psi \sin 2\Phi_0\right] \tag{4.27}$$

$$A_2 = h_0 \sin\zeta \sin^2\theta \left[\frac{1}{2}(1+\cos^2\iota)\sin 2\psi \cos 2\Phi_0 + \cos\iota \cos 2\psi \sin 2\Phi_0\right] \tag{4.28}$$

$$A_3 = h_0 \sin\zeta \sin^2\theta \left[-\frac{1}{2}(1+\cos^2\iota)\cos 2\psi \sin 2\Phi_0 - \cos\iota \sin 2\psi \cos 2\Phi_0\right] \tag{4.29}$$

$$A_4 = h_0 \sin\zeta \sin^2\theta \left[-\frac{1}{2}(1+\cos^2\iota)\sin 2\psi \sin 2\Phi_0 + \cos\iota \cos 2\psi \cos 2\Phi_0\right] \tag{4.30}$$

The time dependent functions $h_i(t)$ used in eq. (4.26) have the form

$$h_1(t) = a(t)\cos 2\Phi(t) \tag{4.31}$$

$$h_2(t) = b(t)\cos 2\Phi(t) \tag{4.32}$$

$$h_3(t) = a(t)\sin 2\Phi(t) \tag{4.33}$$

$$h_4(t) = b(t)\sin 2\Phi(t) \tag{4.34}$$

being $a(t)$ and $b(t)$ the same used in eqs. (4.17) and (4.18), and $\Phi(t)$ In the frequency domain, the gravitational wave signal has a carrier frequency of $2f_0$ that is amplitude and phase modulated. The amplitude modulation splits the carrier into five lines corresponding to frequencies $2f_0 - 2f_r$, $2f_0 - f_r$, $2f_0$, $2f_0 + f_r$ and $2f_0 + 2f_r$, being $f_r \simeq 10^{-5}$ Hz the Earth rotation frequency.

Given this precise knowledge of the expression of the amplitude modulation, this effect can be easily taken into account by applying a matched filter on the spectrum of the signal [38].

4.3 Data analysis techniques

As already pointed out in section 4.1, performing a blind all-sky search for continuous waves is quite difficult because the effect of the phase modulation depends on many unknown parameters.

A possible method of analysis is called *coherent search*. This is a procedure in which one can discretize the parameter space, and then perform the demodulation for each point. However, the number of these points is very high, and scales as T^4 [11]. This means that, for long observation time T, the time required to perform the analysis would largely exceed the observation time itself. To avoid this, a coherent search could not be performed for an observation time longer than a few days.

A possible solution to this computational problem is to use an alternative procedure, dividing the observation time into shorter segments. This

method is called *incoherent search*, because the phase information between two different segments is lost. This consists in splitting the observation time T into N stacks of length T_{stack}, chosen so that a coherent search over this time is feasible. The output of each coherent search performed over one stack is a collection of functions $\tilde{h}(f)$, one for each value of the parameter space, that are quadratically added over the N stacks. It can be shown that the time required for an incoherent search is smaller than that required for a coherent search by a quantity

$$\tau_{inc} \simeq \frac{1}{N^{n-1}} \tau_{coh} \tag{4.35}$$

where the power n represents the dimention of the parameter space, and it depends on the kind of pulsar observed [11]. Before adding the power spectra related to the stacks, each has to be demodulated for the Doppler effect. In alternative, one can choose T_{stack} short enough to consider the phase modulation negligible, reducing the computational time. However, longer stacks imply better sensitivity, though with more expensive computational time. Several variations of this scheme can be applied in order to increase its efficiency [38].

However, this is not the only way available to improve computational time for the continuous wave analysis. In the next chapter we will introduce a new algorithm that performs a fast correction of the phase modulation through a discrete resampling of the signal.

Chapter 5

Resampling algorithm for semi-targeted search

As already mentioned several times, the continuous gravitational signal search requires long integration time in order to dig out the very small signal from the instrumental noise floor. We have also seen that this type of search needs the knowledge of several source parameters (frequency, spin-down and direction) to recover the monochromatic peak smeared by Doppler effect and source slowing down. Each unknown parameter weights on the computational cost, and traditional technique computational time exceeds the observation time itself, even by orders of magnitude.

The method illustrated in this chapter is computationally very effective. The goal is to reduce the number of frequencies over which the signal energy is spread due to the Doppler and spindown effects into a single frequency corresponding to the source one, and then perform the analysis using the Fast Fourier Transform algorithm. The idea is to correct for the Doppler effect by a fast resampling that removes or doubles single samples in a timely manner in order to keep the detector time synchronized with the source one with a large accuracy.

5.1 Doppler correction by discrete resampling technique

In sec. (4.1) it was shown that the Doppler effect can be corrected by resampling the antenna signal using a modified time $t' = t + \frac{\vec{x}(t)\cdot\hat{r}}{c}$ so to recover a pure sinusoidal signal.

Let us introduce our method considering a source in a given position of the sky. One can figure out that this source emits a monochromatic wave at a frequency equal to the sampling frequency of the antenna ν_s (for instance, in Virgo this frequency is 20 kHz). This is not a realistic case, but it is necessary for introduce our technique. Its equiphase planes are orthogonal to the wave vector $\vec{k_s} = \hat{n}\omega_s/c$, being $\omega_s = 2\pi\nu_s$ and $\hat{n}$ the wave propagation versor, and they travel at the speed of light [36]. In the reference frame at rest relatively to the source, the plane equation for a given phase ϕ is given by:

$$\vec{k_s} \cdot \vec{r} - \omega_s t = \phi. \tag{5.1}$$

Let us take as a reference the family of planes whose phase ϕ is an integer multiple of 2π. They travel parallel to each other, separated by a distance $c\Delta t$, as it can be seen from eq. (5.1). The dephasing between two contiguous equiphase planes is then $\omega_s \Delta t$. An observer at rest with respect to the source that monitors the position of the family of equiphase planes at the sampling frequency would see, at a given sampling time, each equiphase plane taking the place occupied by its predecessor at the previous sampling time. This means that, although these equiphase planes at 2π phase-distance from each other are moving at the speed of light, the positions of their family monitored at each sampling time is always the same. As a consequence, they set a reference grid of planes in the rest frame (a schematic representation of this grid is shown in Fig. (5.1)).

The antenna motion with respect to this reference frame is described by

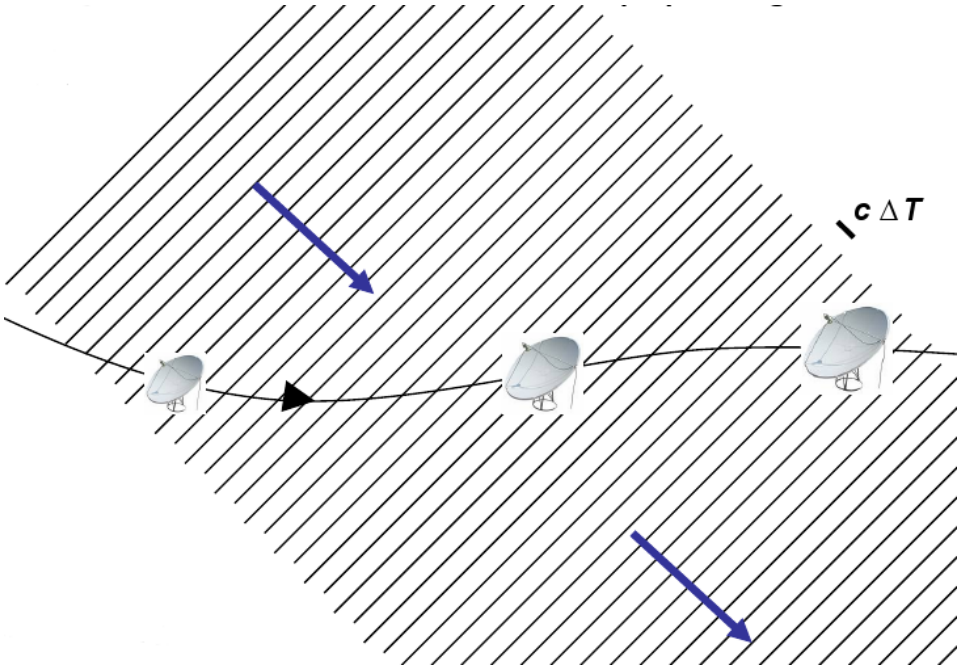

Figure 5.1: *A schematic representation of the equiphase plane reference grid crossed by the antenna during its motion. The distance between two contiguous planes is $c\Delta t$, being Δt the sampling time.*

the trajectory $\vec{r}(t)$. The goal is to synchronize the antenna clock with the source one, in order to have a time difference between them not larger than the sampling time Δt. We can assume, without loss of generality, that the two clocks are synchronized to $\phi = 0$ on the target plane crossing the rest frame origin, coincident with the moving observer starting position fixed at the beginning of the analysis period. The phase measured at time t by the moving observer is given by eq. (5.1), while the one measured by the observer at rest is simply $\omega_s t$. The dephasing due to the motion is then given by $\vec{k}_s \cdot \vec{r}$, and depends only on the antenna position with respect to the reference frame origin.

Each time the moving observer trajectory crosses an equiphase plane, it cumulates a dephasing $\omega_s \Delta t$ relatively to the rest observer. If the antenna

motion versus is opposite to the wave one, i.e. if $\vec{v}(t) \cdot \hat{n} < 0$, the dephasing with respect to the source clock is negative, and the moving observer time is anticipated relatively to the source one. This means that we need to delay the antenna time, in order to keep it synchronized with the source time. The needed delay is then simply obtained by repeating a sample of the signal detected by the moving observer. Similarly, if $\vec{v}(t) \cdot \hat{n} > 0$ a positive dephasing occurs, and the consequent delay in the antenna time relatively to the source one is compensated by removing a sample. Performing this operation each time the antenna trajectory crosses an equiphase plane, the lack of synchronization by the moving observer during its trajectory will not exceed the one existing between two contiguous equiphase planes, namely Δt.

As mentioned in sec. (4.1), if one is able to reduce the phase modulation index below 1 rad applying a correction for the Doppler effect, the first term of the expansion in Bessel functions of the signal keeps more than 75% of the signal amplitude, and thus the peak spectral amplitude reduction with respect to the rest frame will be small [36]. Let us now consider a physical monochromatic signal coming from the source with frequency ν_0. The phase synchronization corresponding to the time one just achieved will be of $\omega_0 \Delta t = 2\pi\nu_0/\nu_s$. If one requires a sky direction knowledge below 1 rad, the sampling frequency has thus to be larger than $2\pi\nu_0$. Being the gravitational wave antenna sampling frequency usually around 20 kHz, this technique can thus be applied to a wide range of source frequencies. The 1 rad accuracy obtained performing the correction for a given sky direction is valid for all the sources in the same direction with frequency $\nu < \nu_s/2\pi$. As a consequence one can assume the Doppler phase modulation corrected for all this frequency range (up to several kHz in the case of Virgo detector). It is important to stress that below a few hundreds of Hz (the region where the continuous wave signals are expected) the accuracy of phase synchronization

$(2\pi\nu_0/\nu_s)$ is much better than 1 rad if $\nu_s = 20$ kHz. This makes the energy losses essentially negligible. In conclusion, one can tune the sampling frequency where our resampling technique is applied as a function of the maximum source frequency to be investigated and to the required accuracy.

One can estimate how many times typically a sample has to be duplicated or removed during a given observation time to keep the time synchronization. Assuming that the moving observer velocity does not change much between two contiguous plane crosses, the time interval is approximated by [36]:

$$t_{cross} = \frac{1}{|\vec{\beta} \cdot \hat{n}|\nu_s} \tag{5.2}$$

where $\vec{\beta} = \vec{v}/c$. In the special case when the antenna moves parallel to the wave, t_{cross} assumes its minimum value $t_{cross} = 1/(\beta\nu_s)$. In terms of samples, the correction cannot occur more often than $1/\beta$ samples, independently of the sampling frequency. Let us notice that for the Earth $\beta \sim 10^{-4}$, therefore we will need to modify just one sample each about ten thousands in antenna digitized signal.

5.2 Preliminary tests

All the information necessary to the signal resampling is stored in a buffer called *mask*. In the simplest scheme, the mask can be seen as an array of N_s integer, where N_s is the number of samples in the original signal. Its values can be either +1, 0 or -1, depending on the action to perform on the corresponding sample: +1 for doubling, -1 for removing and 0 if the sample needs no action. The sampling frequency is not modified by the application of the correction.

The original resampling idea was tested by developing a C language simulation. The routine computed all times t_j the circular orbit used for this preliminary test crosses an equiphase plane of the grid. All values of t_j, expressed in term of the rest frame sample index, and a label indicating the

corresponding action (-1 for sample suppression and $+1$ for duplication) were stored in a two column ascii file (`mask.dat`) [36]. During the data reading the correction is applied simply suppressing (or doubling) single samples (each a few thousands, in realistic cases) according to what written in `mask.dat`. This technique has been tested for several sampling and signal frequencies, wave direction and orbital motion. Fig. (5.2) shows the phase difference between the signal detected by the moving observer and the rest one as a function of the orbital position $x - y$. The same plot for the corrected signal (red points) is close to zero in any orbital position. The residual dephasing (Fig. (5.3)) is contained in a range $\simeq \pm 0.62$ rad (as expected by the phase accuracy relation $\Delta\phi \leq 2\pi\nu_0/\nu_s$). As shown in Fig. (5.4) the correction technique allows to restore a large part of the signal energy, spread by the observer motion on a wide frequency band, in the main spectral bin. The peak recovering has the side effect of increasing the tail amplitude with respect to the case without Doppler correction. This effect is induced by the sawtooth waveform of the corrected phase. Once the mask is computed, all the informations necessary to correct the signal for the Doppler effect are available.

5.3 Spindown correction

The preliminary tests on a circular orbit were performed by considering a monochromatic source with constant frequency. In the real case of a rotating Neutron Star the electromagnetic and gravitational emissions decrease its rotational energy. The Taylor expansion of the Pulsar frequency was already written in eq. (4.16). The cumulated phase is obtained by integrating $\nu(t)$ over time:

$$\varphi(t) = 2\pi \int_0^t \nu(\tau) d\tau = 2\pi \left(\nu_0 t + \frac{1}{2}\dot{\nu}_0 t^2 + \frac{1}{6}\ddot{\nu}_0 t^3 + ... \right). \qquad (5.3)$$

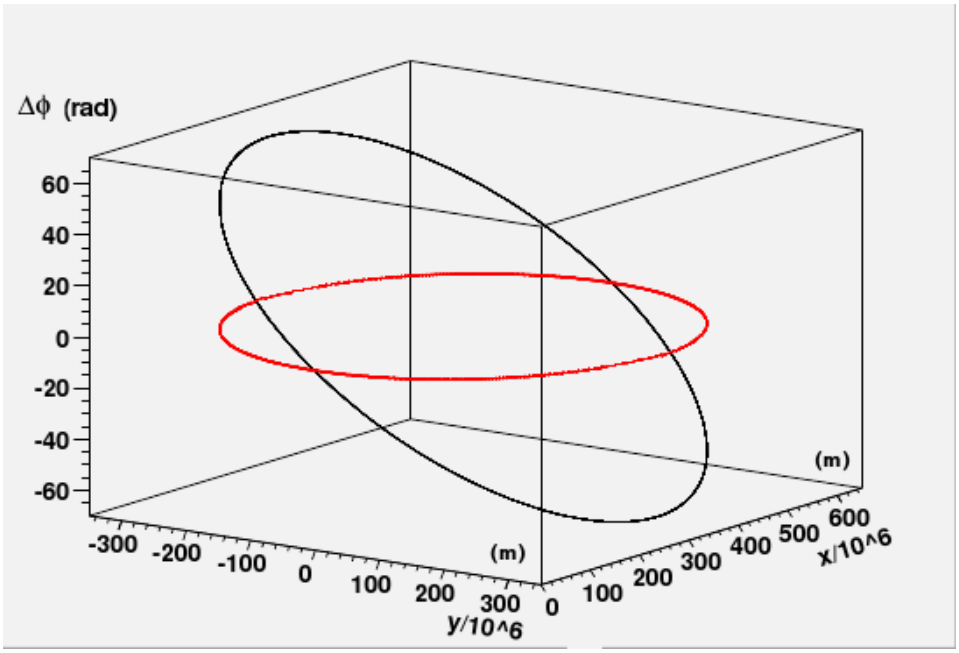

Figure 5.2: *Phase difference between the sinusoidal wave as detected by the moving observer with respect to rest observer as a function of the antenna orbital position x-y (black points). The same plot for the residual dephasing between the corrected signal and the one detected by the rest observer is displayed (red points). INPUT PARAMETERS:* $\nu_0 = 10$ *Hz,* $\nu_s = 100$ *Hz, wave direction :* $n_x = 0$, $n_y = -1$, $n_z = 0$, $R = 3{\cdot}10^8$ *m,* $\beta = v/c = 10^{-3}$.

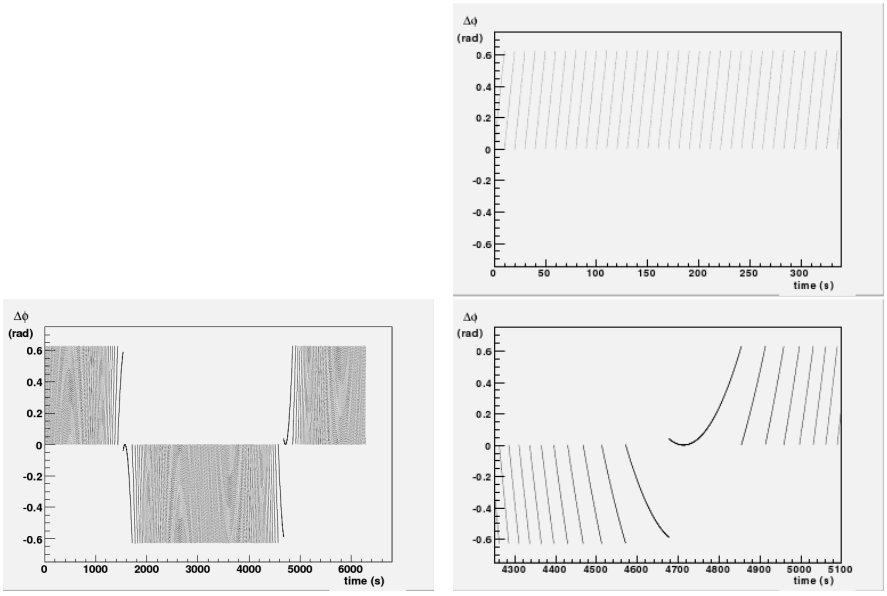

Figure 5.3: *Same phase difference in red points of Fig. (5.2), plotted as a function of time for the entire orbit ($\simeq 6,283$ s). Two zooms of the previous plot around t=0 and t=3/4 of the orbital period are reported. At the beginning (first zoom), when the antenna motion is parallel to the wave, the corrections took place frequently and the residual phase error exhibits the sawtooth shape. Close to the point where the antenna changes versus with respect to the wave vector (zoom 2), the plane crossing (and thus the phase correction) are less frequent.*

We can take the first term of this expansion to write the signal emitted by a Pulsar as

$$S(t) = h_0 \sin\left(\omega_0 t + \frac{1}{2}\dot{\omega}_0 t^2\right) \tag{5.4}$$

where $\omega_0 = 2\pi\nu_0$ and $\dot{\omega}_0 = 2\pi\dot{\nu}_0$, with typical values of $\dot{\nu}$ between 10^{-9} and 10^{-14} Hz/s. The phase of this signal is seen by the moving antenna as

$$\varphi'(t) = \omega_0\left(\frac{\vec{r}(t)\cdot\hat{n}}{c} + t\right) + \frac{1}{2}\dot{\omega}_0\left(\frac{\vec{r}(t)\cdot\hat{n}}{c} + t\right)^2 \tag{5.5}$$

due to the Doppler effect. Since the presence of the spindown term implies that the source frequency decreases in time, it is clear that $\dot{\nu}_0 < 0$.

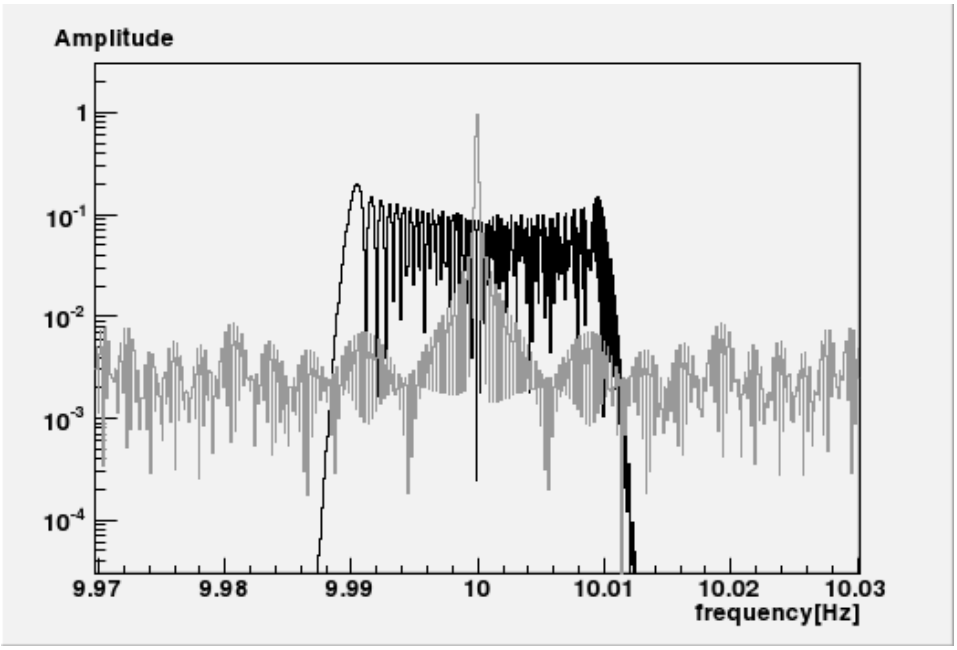

Figure 5.4: *Linear spectral density of the signal as measured by the moving observer (black) and of the corrected signal (gray). The configuration is the same of the previous figure. The energy of the signal detected in moving observer is spread out on many bins. The spectral peak amplitude measured by the rest observer (equal to 1) is almost entirely recovered by the correction technique (peak linear spectral density is about 0.91). An integration time of two orbital periods (about 12,566 s) was considered. Use of log scale was done to emphasize the differences in the tails.*

The frequency spindown introduces a complication in the geometrical approach suggested in the previous section, because the distance between two contiguous equiphase planes is not constant anymore. A geometrical computation of the coordinates at which the antenna trajectory crosses the equiphase planes needs to take into account this time dependence. The change in the phase due to spindown is:

$$\Delta\phi_{sd} = \frac{\dot{\omega}t'^2}{2}, \tag{5.6}$$

while the phase difference between two contiguous planes for a regularly pulsating source is $\omega_0\Delta t = \omega_0/\nu_s$. The time difference cumulated by the moving observer due to spindown is then

$$\Delta t_{sd} = \frac{\Delta\phi_{sd}}{\omega_s} = \frac{\dot{\omega}t'^2}{2\omega_s}. \tag{5.7}$$

5.4 Application to targeted search

In the case of a *targeted search*, for which all the source parameters are known, one can perform the analysis over a very narrow frequency band, downsampling the signal by a new sampling frequency ν'_s. According to the Nyquist theorem, the downsampling frequency has to be at least two times the signal bandwidth. Given that the shift of Pulsar frequency due to its slowing down is very small, a bandwidth of a fraction of Hz is more than sufficient for our purposes. Since the original sampling frequency considered in our work is $\nu_s = 4$ kHz, one can thus downsample the original signal by a factor larger than about 10^4. One can thus choose a time interval ΔT equal to the inverse of the downsampling frequency and calculate how many equiphase planes are crossed by the antenna trajectory during ΔT. The distance travelled by the antenna in this time interval can be well approximated by the projection of the antenna velocity over $\hat{n}$ multiplied by the time interval ΔT. Since the distance between two contiguous planes is

$c\Delta t = c/\nu_s$, the number of plane crossed each ΔT is

$$N_{planes} = \frac{(\vec{v}(t) \cdot \hat{n})\Delta T}{c/\nu_s}. \tag{5.8}$$

The correction to the Doppler phase modulation thus can be performed by computing N_{planes} each ΔT. The resampling mask computation can be usefully re-adapted to the case of a downsampled signal for targeted search. Instead of considering the action to be performed sample by sample, one can actually compute the number of equiphase planes crossed by the antenna trajectory at each downsampling time, and store it in the mask. The number of elements stored in the mask will not be equal to the original signal one (N_s), but instead it will be $N_m = N_s \cdot \nu'_s/\nu_s$. Then the downsampling is made by shifting the sample selection by the amount indicated by the mask. More precisely, the k^{th} sample of the downsampled stream has to be taken from the high-frequency stream in the position

$$S'_k = S_k + M_k \tag{5.9}$$

where S_k is the sample that would be taken in absence of correction and M_k is the k^{th} element of the mask. For instance, if our downsampling time is 100 s (meaning a downsampling frequency of 10^{-2} Hz), instead of the $k \cdot 100\ s \cdot 4$ kHz sample one has to fill the downsampled buffer with the $k \cdot 100\ s \cdot 4$ kHz $+M_k$ sample of the 4 kHz data stream to recover the synchronization.

The action that has to be performed is specified by the mask sign. If $M_i > 0$ then the scalar product between $\vec{v}(t)$ and $\hat{n}$ is positive, and one has to move forward of M_i samples in order to obtain the effect of removing samples while performing the downsampling. In the opposite case we have to move backward of M_i samples, which is the same as adding M_i samples in the original high-frequency signal. This resampling method is illustrated in Fig. (5.5). The number of target planes crossed each ΔT is computed as indicated by eq. (5.8). The antenna velocity $\vec{v}(t)$ is obtained by interpolation

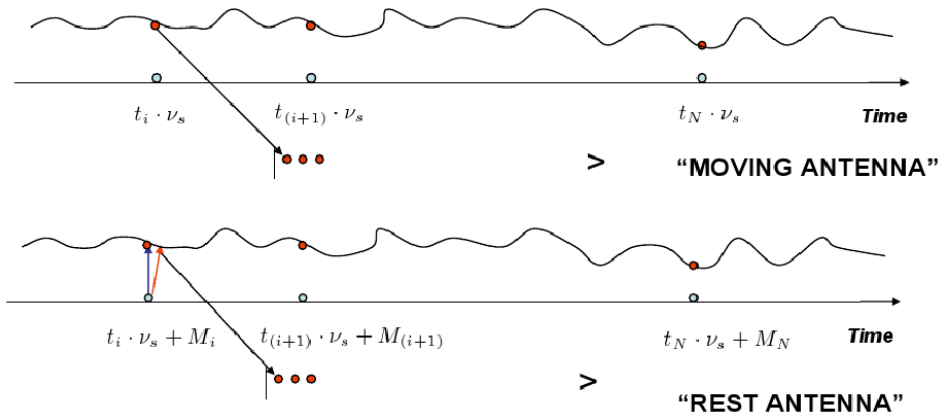

Figure 5.5: *The resampling method: the buffer of the downsampled stream is filled taking from the high-frequency stream the sample shifted with respect to the one without correction, by the amount of samples indicated by the mask. A backward shift introduces a delay in the antenna clock, while a forward shift has the opposite effect.*

from 1 s sampled ephemeris[1] at time $t = t_0 + i\Delta T$. One can assume without loss of generality that the analysis starts at time $t_0 = 0$, and compute the distance $\vec{r}(t)$ with respect to the position at the starting time $\vec{r}(t = 0)$ in the SSB coordinates.

A term has to be inserted in eq. (5.8) in order to correct the plane drift. The amount of samples cumulated because of the source slowing is obtained by eq. (5.7):

$$\Delta N_{sd} = \frac{\dot{\omega} t'^2}{4\pi}. \tag{5.10}$$

The i^{th} mask value can be computed using this result, obtaining:

$$M_i = \frac{(\vec{v}(t) \cdot \hat{n})\Delta T}{c/\nu_s} + \Delta N_{sd}. \tag{5.11}$$

N_{planes} needs a further correction due to the time that the wavefront needs

[1]The Virgo antenna trajectory in SSB was given by *PSS* libraries, developed at INFN Roma 1 [39]. These routines make use of the NOVA satellite for the generation of precise ephemeris [37].

to cross the target planes. This effect is compensated by repeating the calculation of M_i, performing an iteration over the time, with a certain computational cost. The method described above is based on geometrical considerations about the antenna trajectory.

In the case of the targeted search a way to solve the spindown problem is to choose a downsampling time t_0 and then find the value of time t' at which the moving observer phase $\varphi'(t')$ is equal to the rest observer one at the downsampling time in the case of a monochromatic source with constant frequency. This means to impose:

$$\omega_0 \left(\frac{\vec{r}(t') \cdot \hat{n}}{c} + t' \right) + \frac{1}{2}\dot{\omega}_0 \left(\frac{\vec{r}(t') \cdot \hat{n}}{c} + t' \right)^2 = \omega_0 k t_0 \qquad k = 1, \dots T/t_0 \tag{5.12}$$

with the usual notation, and where T is the whole observation time. $t' - kt_0$ represents thus the time difference between the two reference frames. The number of samples to be modified in order to synchronize the two clocks is given by

$$N_S = (t' - kt_0)\nu_s. \tag{5.13}$$

Since this correction equalizes the two phases, it includes simultaneously both the spindown and the Doppler effects. Solving eq. (5.12), we obtain the time shift between the moving observer and the rest one:

$$\delta t = t' - kt_0 = -\frac{\vec{r}(t') \cdot \hat{n}}{c} + \frac{\varepsilon (kt_0)^2}{1 - \varepsilon k t_0 + \sqrt{1 - 2\varepsilon k t_0}} \tag{5.14}$$

where $\varepsilon = \dot{\nu}_0/\nu_0$ is the *fractional spindown*. It is important to stress that one has to compute δt only few times over the observation time (each downsampling time), and the applied correction is valid for all the sources in the $\hat{n}$ direction with the same value of ε. As already mentioned, the main difficulty with this approach consists in the dependence of the time shift δt on the position $\vec{r}(t')$, with t' unknown. The solution is obtained numerically by iterations. We first evaluate eq. (5.14) considering the antenna position at

the not corrected sampling time $\vec{r}(t_0)$, and then we repeat the computation replacing t_0 with $t_0 + \delta t$ until the result converges. The i^{th} value stored in the mask is thus obtained by

$$M_i = \delta t \cdot \nu_s. \tag{5.15}$$

This approach, based on the analytical solution of the problem of finding the time at which the antenna receives the same signal phase as the one seen at a given time t_0 by an observer at rest with respect to the source, turned out to be more clean and effective than the geometrical one because the spindown correction is included from the beginning.

The first two techniques considered are both based on the idea of correcting the signal while downsampling it. The downsampling method has already been outlined in the previous section, and it is clearly represented in Fig. (5.5). Our routines are applied over binary data files, that allow us to surf between the samples in a fast way. We reach through a `for` cycle the sample that would be selected by a simple downsampling (i.e. one sample each without correction), and then we use the C built-in function `fseek` to pick up the shifted sample. The number of data that `fseek` has to skip is the one stored in the mask. Once written the selected sample in an output buffer, we jump to the next "non-corrected sample". The large amount of data that we have to analyse requires to be splitted over several files[2].

5.5 Validation of the technique

Several tests of the resampling method have been performed. We simulated signals considering many different values of signal frequency ν_0, sampling

[2] A jump from a file to another can therefore occur, and our routine has to be able to work in such situations. We define thus a *threshold* to check if we are near to one of the file ends, in order to manage in an effective way the fact that a corrected sample can be out of the considered file.

frequency ν_s and spindown $\dot{\nu}_0$, several source directions and even many orbital parameters (two different circular orbits and ephemeris for the first Virgo Scientific Run), while the source amplitude modulation is still not considered. The technique turned out to be very effective.

In order to check the phase locking we produced by an external routine two sinusoidal signals: one with phase $\omega_0 t$ (*rest signal*) and one with phase $\omega_0 \left(\frac{\vec{r}(t)\cdot\hat{n}}{c} + t\right) + \frac{1}{2}\dot{\omega}_0 \left(\frac{\vec{r}(t)\cdot\hat{n}}{c} + t\right)^2$ (*modulated signal*). A comparison was performed before and after applying the correction to the latter.

First of all the phase locking accuracy was tested. The tests performed with the circular orbits let us show the robustness of the technique using a short time. We repeated the test on two orbits with the following parameters:

	Orbit 1	Orbit 2
R (m)	$1.5 \cdot 10^8$	$1.5 \cdot 10^{10}$
β	10^{-4}	10^{-4}

Table 5.1: *Parameters of the circular orbits used in the first tests: R is the orbital radius, β is the ratio between the orbital velocity and c.*

We considered also various spindown values, choosing a physical one ($\dot{\nu}_0 = 10^{-11}$) and a non-physical one ($\dot{\nu}_0 = 10^{-7}$). In both cases the signal phase was correctly recovered, with a dephasing between the rest signal and the corrected one that does not exceed the predicted limit of $2\pi\nu_0/\nu_s$ (see sec. (5.1)). Fig. (5.6) shows the difference in the phase between the rest signal and the corrected one for Orbit 1 over $3 \cdot 10^5$ s (more than three days), with $\nu_0 = 20$ Hz, $\dot{\nu}_0 = 10^{-11}$ Hz/s and $\nu_s = 1000$ Hz. The plot shows the expected phase locking accuarcy of 0.126. The same result have been obtained for Orbit 2, with both a physical spindown ($\dot{\nu} = 10^{-11}$, in Fig. (5.7)) and a non-physical one ($\dot{\nu} = 10^{-7}$, in Fig. (5.8)).

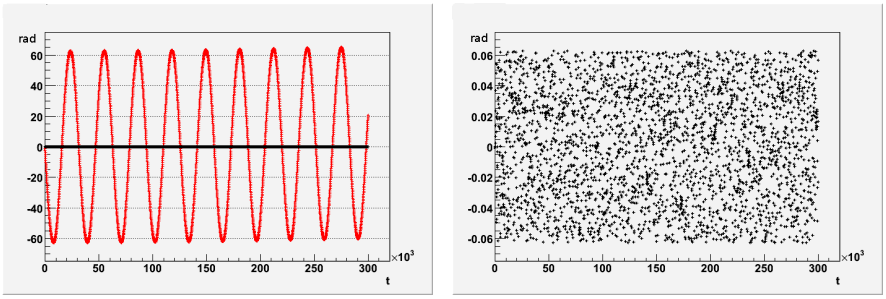

Figure 5.6: *Phase locking accuracy test using Orbit 1. The plot on the left shows the phase difference between the rest signal and the modulated one (red curve) and the one between rest and corrected signals (black curve). The signal modulation due to the Doppler effect and the small drift due to spindown are evident in the red curve. The maximum dephasing after the correction visible in the y axis zoom of the black curve is the one expected:* $2\pi\nu_0/\nu_s = 0.126$.

Once the method has been tested on the circular orbit, we performed other tests with the ephemeris orbit, i.e. with the real antenna motion in the SSB during VSR1. Fig. (5.9) shows an example of the test performed for five days long data with $\nu_0 = 25$ Hz, $\dot{\nu} = 10^{-11}$ Hz/s and $\nu_s = 1$ kHz. Also in this case the dephasing is the one expected.

Once established the method accuracy in phase locking, we estimated also the peak amplitude recovering in the signal spectrum for various frequencies ν_0, spindown values $\dot{\nu}$ and sampling frequencies ν_s (400 Hz, 1 kHz and 4 kHz). An example of a corrected signal spectrum compared to the one without correction is shown in Fig. (5.10). The results of the comparison between different sampling frequencies are shown in Fig. (5.11) and (5.12), from which it is clear that the peak amplitude recovery depends only on the ratio ν_0/ν_s as expected. We are mainly interested in $\nu_0/\nu_s < \pi/2$ in order to keep the phase accuracy below 1 rad. In this situation, the percentage of peak amplitude losses is very small (under 5%). We are therefore allowed to use low sampling frequencies as long as the phase accuracy remains below 1

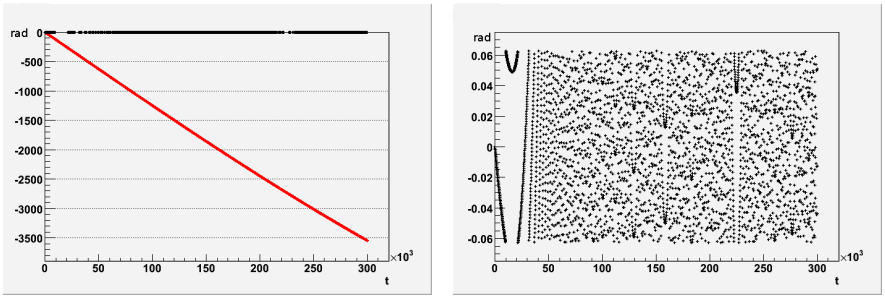

Figure 5.7: *Phase locking accuracy test using Orbit 2. The plot on the left shows the phase difference between the rest signal and the modulated one (red curve) and the one between rest and corrected signals (black curve). The y axis zoom of the black curve shows that the maximum dephasing after the correction is the one expected:* $2\pi\nu_0/\nu_s = 0.126$.

rad, without incurring remarkable peak amplitude losses, as it is shown in Figs (5.11) and (5.12).

All the tests performed show that the method is really effective in the correction of the phase modulation induced by Doppler and spindown effects. The method is also computationally effective. In Tab. (5.2) we show the computing times obtained in the preliminary tests described so far to process 5 days of data. The computing times directly related to the resampling

ν_s (Hz)	Mask computation (s)	Mask application (s)	Total (s)
4000	0.28	2.5	20.67

Table 5.2: *Computing times for* $\nu_s = 4$ *kHz, over a signal during 5 days. All the values are obtained as a mean over 10 measures.*

method (calculation and application of the correction) can be distinguished from the total computing time. The residual time is a fix cost that we pay for I/O operations (file opening, reading and writing), that would be unavoidable for any analysis pipeline. From the shown results we can say that this search method takes about 10^{-4} of the real time to perform the

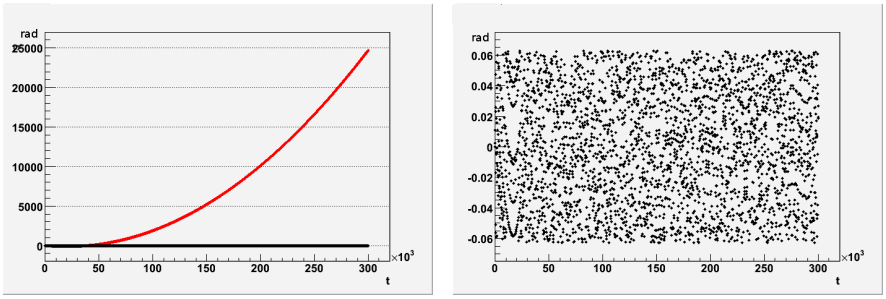

Figure 5.8: *Phase locking accuracy test using Orbit 2 and a very strong spindown ($\dot{\nu} = 10^{-7}$). The plot on the left shows the phase difference between the rest signal and the modulated one (red curve) and the one between rest and corrected signals (black curve). The plot on the right shows that the maximum dephasing after the correction is the one expected:* $2\pi\nu_0/\nu_s = 0.126$.

correction. This result can still be improved by future optimizations and by reducing the starting sampling frequency, that is now higher than necessary to guarantee a peak reconstruction with the required accuracy.

5.6 The pipeline

After the validation, we applied the technique to a part of the VSR1 data.

The VSR1 data were divided in many segments of various length (from a few thousands to a few hundred thousands of seconds). The data segments are not contiguous, because of interruptions during the run data taking. We replaced the missing data frames with zeroes (*zero-padding*) in order to keep the correct phase in the data. The steps in the data induced by the zero-padding are smoothed by the windowing factor $\sin^2(\frac{1}{2}\pi t/t_{win})$, where t_{win} is the windowing time, typically of tens of seconds. This operation is necessary in order to avoid the presence of spurious effects induced by the steps, especially during the filtering.

We used the 4 kHz sampled data of the gravitational wave amplitude

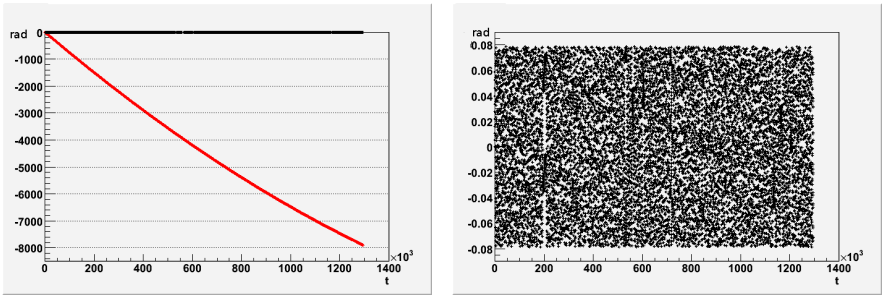

Figure 5.9: *Phase locking accuracy test using ephemeris and $\dot{\nu} = 10^{-11}$ Hz/s. The plot on the left shows the phase difference between the rest and the modulated signal (red curve) and the one between rest and corrected signals (black curve). As it can be better appreciated from the zoom of the black curve on y axis, the maximum dephasing after correction for a signal with $\nu_0 = 25$ Hz and $\nu_s = 1000$ Hz is ~ 0.157, as expected.*

measurement of the $h(t)$ as provided by Virgo calibration group. The process of zero-padding and windowing are parallel to the data filtering. A band-pass filter is applied around a given central frequency to 4 kHz data. The band-pass filter used is a type II Chebyshev filter of the 9^{th} order, with a gain $A = 100$ dB. This choice was due to the characteristics of no ripples in the passband of this type of filter. The filter cuts all the negative frequencies to avoid aliasing in the spectrum, so the filter output consists of complex elements. We applied the resampling to a set of two days data filtered by a pass-band Chebyshev filter with cutoff frequency $\nu_{stop} = 0.05$ Hz, centered around $f_0 = 30.445$ Hz. The Doppler and spindown correction downsampling was then applied to the 4 kHz filtered signal. In particular, the filtered data were undersampled, corrected by mask application using the technique described in sec. (5.4), and a heterodyne was applied to bring them to the baseband. These three operations are made in a single step. The FFT was then performed on the downsampled data, and thus with a reduced number of samples. The plot of the obtained spectrum is shown in Fig. (5.13). As one can see from the comparison of the two plots, the

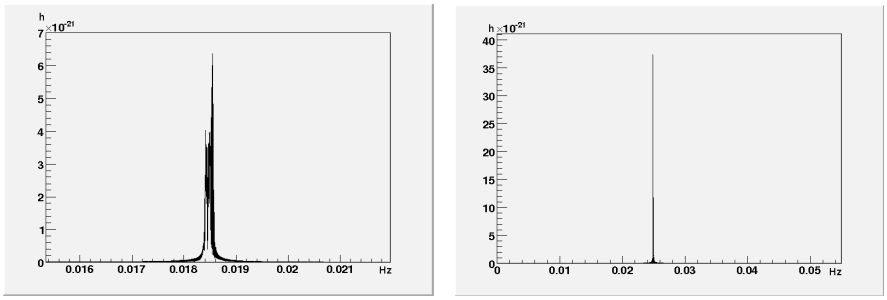

Figure 5.10: *On the left: amplitude of the signal spectrum by a source with* $\nu_s = 4$ *kHz,* $\nu_0 = 30.025$ *Hz and* $\dot{\nu} = 0.5 \cdot 10^{-11}$ *Hz/s, filtered by a Chebyshev passband centered around 30 Hz, downsampled at* $\nu'_s = 0.1$ *Hz and brought to the baseband. The Doppler smearing is clearly visible. On the right: amplitude spectrum of the same signal, corrected for the Doppler and spindown effects. The peak amplitude loss after reconstruction is less than* 1%.

stopband noise is increased by the mask application by a small factor that is visible only outside of the filter passband. We then filtered a test signal with no noise, with the results shown in Figs (5.14) and (5.15).

5.7 Semi-targeted search

We stress again that our method is valid for all frequencies that satisfy $\nu_0 \leq \nu_s/2\pi$, so the targeted search is just a particularly simple case in which it can be applied. Since this independence of the frequency is the real advantage of the technique, the application to a broadband is very promising in terms of computing costs with respect to other techniques. The band over which the analysis is performed can thus be broadened, allowing the search of possibly existing sources emitting in that frequency band (*semi-targeted search*).

Since Virgo is the unique detector in action to exhibit a good sensitivity also in the low-frequency range (i.e. below a few tens of Hz), we

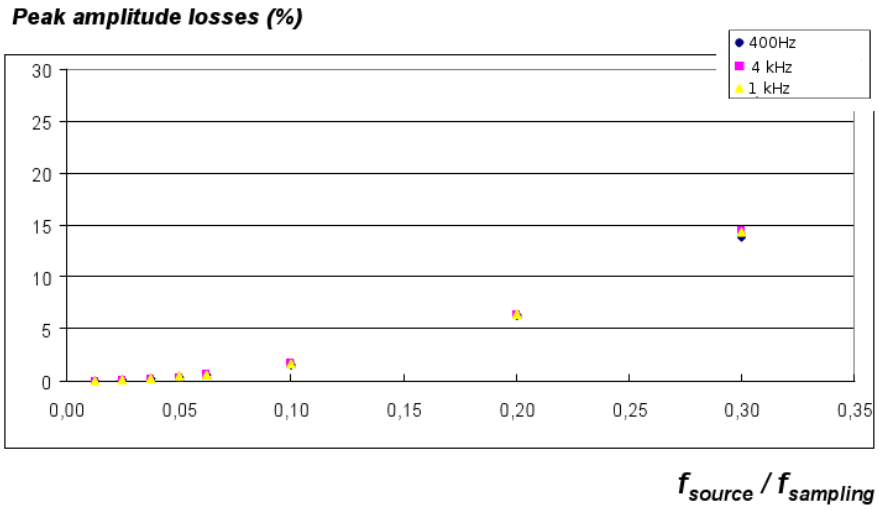

Figure 5.11: *Peak amplitude losses percentage versus the frequency ratio ν_0/ν_s for three different sampling frequencies. The losses depend only on the frequency ratio and not directly on ν_s. The estimated errors were smaller than the plot resolution.*

decided to apply our resampling method in the whole band below 50 Hz. A semi-targeted search on a broadband can be performed correcting the signal sample by sample, i.e. recognizing the single samples that have to be doubled or removed, as required by the first conceptual scheme outlined at the beginning of sec. (5.2). In order to identify exactly which samples of the high-frequency stream have to be removed or doubled one can tune eq. (5.12) more precisely by substituting the right-hand term with the maximum dephasing allowed by the technique. The equation to be solved becomes then:

$$\omega_0\left(\frac{\vec{r}(t')\cdot\hat{n}}{c}+t'\right)+\frac{1}{2}\dot{\omega}_0\left(\frac{\vec{r}(t')\cdot\hat{n}}{c}+t'\right)^2=\omega_0 k\Delta t \qquad k=1,\dots T/\Delta t \tag{5.16}$$

where $\Delta t = 1/\nu_s$ is the signal sampling time. The solution in this case is

$$t'=\frac{\varepsilon\left(\frac{\vec{r}(t')\cdot\hat{n}}{c}\right)^2-2\left(\frac{\vec{r}(t')\cdot\hat{n}}{c}-k\Delta t\right)}{1-\varepsilon\frac{\vec{r}(t')\cdot\hat{n}}{c}+\sqrt{1-2\varepsilon k\Delta t}}. \tag{5.17}$$

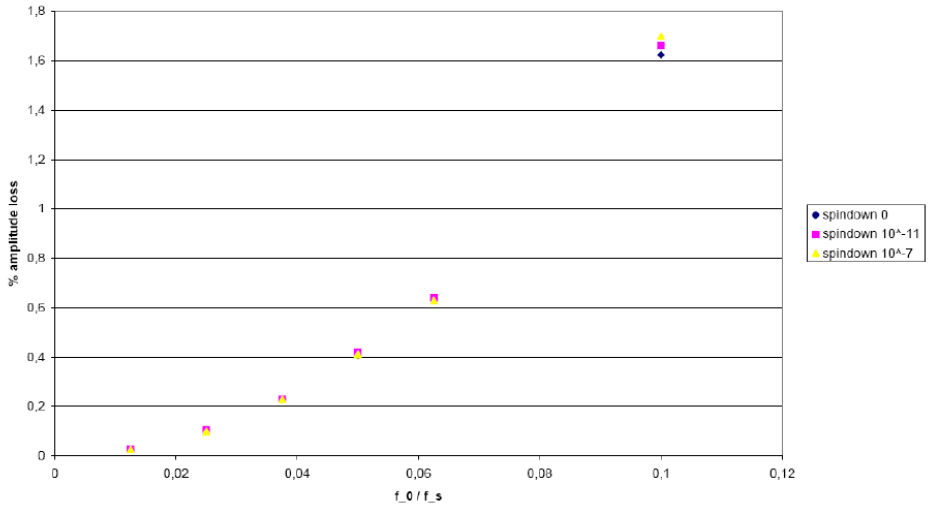

Figure 5.12: *Peak amplitude losses percentage versus the frequency ratio ν_0/ν_s for three different spindown values. The losses do not depend on spindown. The estimated errors were smaller than the plot resolution.*

Applying the correction to a data set with $\nu_s = 250$ Hz, we can obtain a good correction for all source frequencies $\nu_0 \leq \nu_s/2\pi$ (Fig. (5.16)), and thus surely up to 50 Hz.

The scheme for a semi-targeted search can be implemented by calculating the mask using eq. (5.17). As in the targeted case, we need to compute the solution iteratively because of the dependence of t' on $\vec{r}(t')$ (defined in sec. (5.4)). In this case, the evaluation of (5.17) for the first sample is done by starting from an expression without the term depending on ε:

$$t'_{start} = -\frac{\vec{r}(t_0) \cdot \hat{n}}{c}, \tag{5.18}$$

and then we compute the complete expression replacing t_0 with t'_{start}. For the n^{th} sample the process starts using the value of t' obtained for the $(n-1)^{th}$ one. In order to know exactly which samples need the correction, a bisection algorithm was applied. We use the fact that the n^{th} element

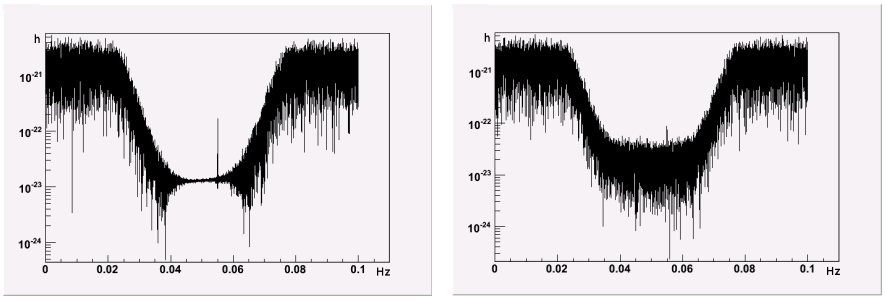

Figure 5.13: *On the left: two days of VSR1 data filtered by the Chebyshev pass-band. On the y axis is shown the modulus of the FFT performed over the complex filter output. On the right: the same data resampled by the mask. In both plots is clearly visible the characteristic filter shape, represented between 0 and 5 Hz instead of -2.5 and +2.5 Hz because we are not considering negative frequencies.*

in the mask differs from the $(n-1)^{th}$ by an amount ± 1 as soon as we find the sample to be corrected. This hypothesis is surely valid for a mask computation sampling of 0.5 s. Since the minimum value for a target plane crossing is 0.5 s (see eq. (5.2)) we are sure that the variation between two contiguous elements of the mask can be only 0, +1 or -1. The classic root-finding algorithm is then modified to find the sample at which the mask changes its value, in analogy with a function that changes its sign immediately after a root. The number of the found samples is then stored into a buffer that will be used for the correction.

The spectral analysis is performed using the C `fftw` library. Since we use a single FFT buffer, the amount of data that can be analyzed is limited by the buffer maximum dimension. An FFT on several buffers could be performed at the prize to reduce the effectiveness of the process. Since we are forced to use at least 100 Hz FFT in order to have a 50 Hz band and the buffer maximum dimension is about $6 \cdot 10^7$, only about 12 hours of data can be analyzed in a single buffer. For a given integration time T, the maximum sampling frequency allowed to have an FFT in a single buffer is connected

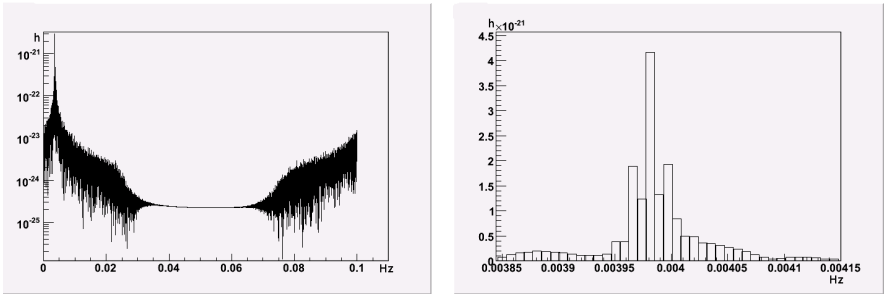

Figure 5.14: *On the left: amplitude spectrum of a sinusoidal signal filtered by the same Chebyshev passband as Fig. (5.13), with* $\nu_0 = 15.223$ *Hz,* $\dot{\nu} = 0.295 \cdot 10^{-10}$ *Hz/s,* $T = 2$ *days and downsampling time* $\Delta t = 10$ *s, zoomed on the right around the signal frequency.*

to the maximum number of elements in the buffer by:

$$\nu_s \leq \frac{N_{FFT,max}}{T}. \tag{5.19}$$

This relation defines then the bandwidth $\Delta\nu_B$ over which we can perform a semi-targeted search of length T, since it needs to satisfy the condition by the Nyquist theorem $\Delta\nu_B \leq \nu_s/2$. This method, that applies the mask on the original data stream with no pass-band filter, can be implemented for wide band searches on long periods if one accepts the idea to perform very long FFT extending the maximum number of points to be analyzed in the spectrum, or to perform FFT using more buffers. Vice versa if one wants to keep the spectral analysis light, using a reasonable number of samples, the band to be investigated has to be reduced. For this reason we decided to use another implementation of the technique based on the previous method (the one for targeted search), but with a broader band. In order to analyze one month long data without exceeding the value of $N_{FFT,max}$ previously mentioned, sampling frequency cannot be larger than 10-20 Hz, meaning a maximum bandwidth of about 5-10 Hz. The analysis was performed over thirty days long data originally sampled with $\nu_s = 4$ kHz, filtered by the previous described Chebyshev pass-band with a cutoff frequency $\nu_{stop} = 2.5$

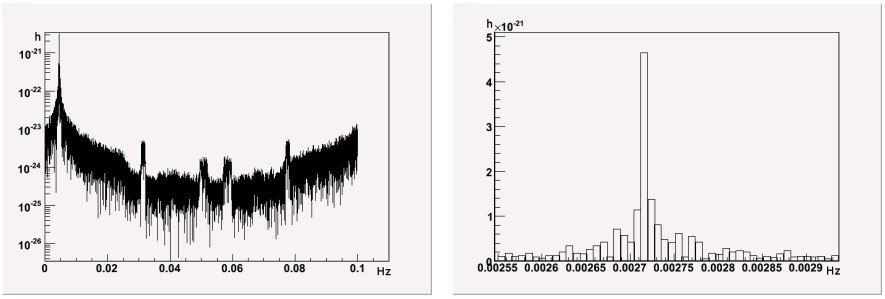

Figure 5.15: *On the left: amplitude spectrum of the same signal of Fig. (5.14) with the mask correction. The zoom on the right shows the narrower, higher peak recovered at the same frequency as the analogous rest peak with an amplitude recovery accuracy of* $\sim 98\%$.

Hz, centered around $\nu_0 = 19.0$ Hz. We injected a modulated signal with $\nu = 20.025$ Hz and $\dot{\nu}/\nu \simeq 5 \cdot 10^{-13}\ s^{-1}$, that was well reconstructed by the application of the technique, as it can be seen in Fig. (5.18). It is important to remark once again that the correction is valid for all frequency bins. Since the integration time is very long (millions of seconds), the frequency resolution is below 1 μHz, and thus millions of bins are corrected at the same time. In this sense a search over a 2.5 Hz band can be considered semi-targeted. The analysis has been performed dividing the whole data stream in 12 hour long segments. The mask computation over each segment took less than 1 s, while the mask application over each segment lasted $\sim$ 27 s, on average. The whole analysis took 1679 s, i.e. $\sim 10^{-4}$ of the data duration. We are confident that a strong reduction of this number, obtained without any special precaution and already good if compared with other pipelines, will take place in the final architecture, where computing optimization and parallelization will be implemented. Given the good results obtained with the technique for the analysis of a single sky direction and a single fractional spindown over one month of data, we can build over it a more complete pipeline parallelizing its application over many values of

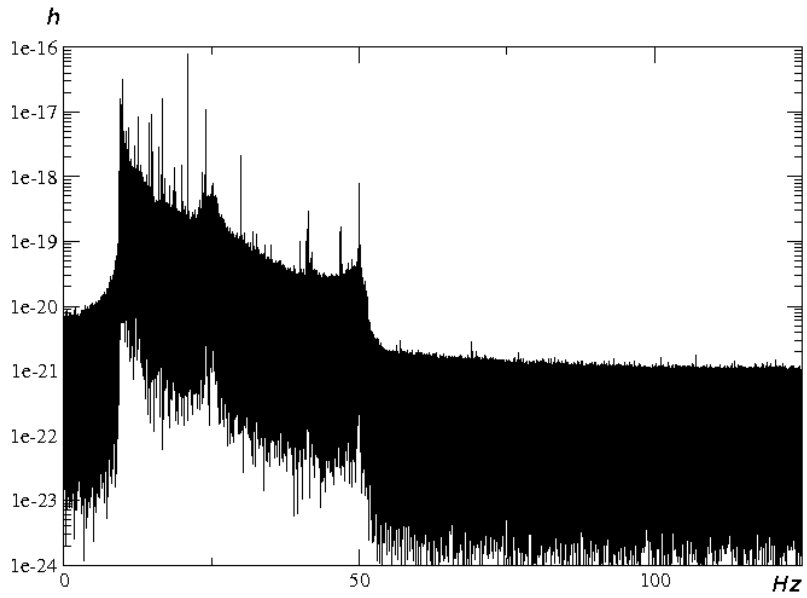

Figure 5.16: *250 Hz Butterworth filtered and corrected data.*

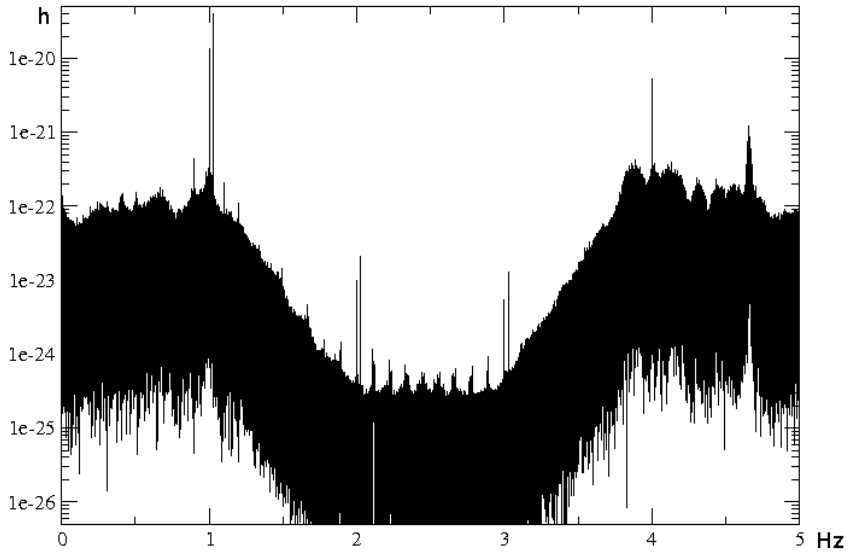

Figure 5.17: *Plot of the spectrum obtained resampling a 30 day long data stream filtered by a Chebyshev pass-band with $\nu_{stop} = 2.5$ Hz and a central frequency $\nu_c = 19.0$, with a signal injected at $\nu = 20.025$ Hz and $\dot{\nu}/\nu \simeq 5 \cdot 10^{-13}\ s^{-1}$ with an amplitude $h_0 = 10^{-19}$. The signal peak at 1.025 Hz is clearly visible near to the peak at 1.0 Hz corresponding to the 20 Hz instrumental line.*

these parameters. The parallelization of the routine will be made by using the Grid technology, a computing infrastructure developed by CERN, that allows to manage huge quantity of data. Through the parallelization, we will be able to use the resampling technique effectiveness over a wide range of sky directions and fractional spindowns.

It is important to remind that the source amplitude modulation (introduced in the previous chapter) was not taken into account. A very effective method to recover from this effect acting in the output spectrum was recently

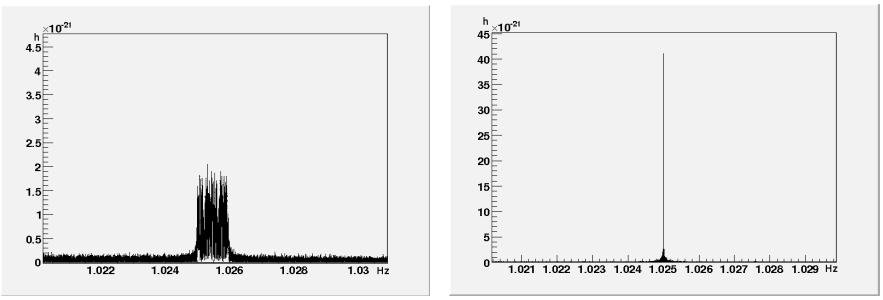

Figure 5.18: *Zoom of the spectrum seen in Fig. (5.17) around the signal injected in the data at 20.025 Hz (and thus appearing at 1.025 Hz in the 19 Hz centered filtered spectrum.). On the left: the smeared signal before the correction. On the right: the corrected signal.*

proposed by Rome INFN group [40]. The effect of the amplitude modulation is a production of two sidebands at the Earth rotational frequency and its double, on both sides of the central frequency. The amplitude of the five lines depends on two parameters only, generally unknown (polarization phase and orbit inclination). Estimators based on simple scalar products at the concerning frequency between the signal spectrum and the recovered experimental one can be used with very small computational costs. In our case, we have to perform this correction (consisting for each source frequency in a few products) moving on the central frequency (unknown in the semi-targeted search) and on the two parameters just mentioned.

Conclusions

In this thesis a new technique for the continuous gravitational wave search was introduced. We have shown that the phase modulation induced in the signal by the Doppler effect, due mainly to the Earth orbital motion, can be corrected by an effective resampling method that synchronizes the antenna clock with the source one. This synchronization is achieved by removing or doubling a few samples of the antenna digitized signal in order to accelerate or slow down in a timely manner the moving clock. The dephasing due to the source frequency slowing because of electromagnetic and gravitational emissions (*spindown*) has also been corrected.

The proposed technique is particularly effective in the cases where source direction is known while the frequency is not (*semi-targeted search*), because it depends only on the spindown parameter $\dot{\nu}/\nu$ and not on the source frequency. In other words, the correction obtained for a given spindown is accurate enough for frequencies smaller than $\nu_s/2\pi$, where ν_s is the sampling frequency, that is enough for usual cases. The peak in the spectrum due to any unknown source in the chosen direction emitting within this frequency band a gravitational signal with remarkable amplitude could be detected after a single correction.

First of all we performed a validation of the technique for a search where all the source parameters are known with high precision (*targeted search*). In this case it was possible to check that a high accuracy in the phase locking between the antenna and the known source signal can be achieved. In

particular we proved that the dephasing due to Doppler effect and spin down were compensated in all cases within the expected limit of $2\pi\nu/\nu_s$, i.e. 2π times the ratio between the source frequency and the sampling one, and that this corresponds to very low losses in the spectral peak amplitude recovery (of the order of a few % in the usual cases). The required computing time turned out to be below 10^{-4} parts of the length of the period under study, which is a very good result if compared with other pipelines developed for continuous gravitational wave searches. Moreover, this number is expected to increase by future optimizations and using particular architectures.

The technique was then applied to semi-targeted search. After several tests using Virgo Scientific run data we concluded that an effective implementation of our technique is to perform the semi-targeted search over a bandwidth of a few Hz. In this way the sampling frequency can be reduced down to the double of the bandwidth and thus a Fast Fourier Transform analysis for peak search over long integration times (months) can be performed with an acceptable number of points. This pipeline is going to be implemented, using the Grid technology, as a parallel analysis over many sky directions and many values of relative spindowns ($\dot{\nu}/\nu$).

Acknowledgments

I would like to thank my supervisors, Isidoro Ferrante and Stefano Braccini, for their guidance and encouragement throughout these months. Thanks also to Sergio Frasca, Cristiano Palomba, Pia Astone and Federica Antonucci by Rome 1 INFN Virgo group for their valuable suggestions and for the help in the use of PSS libraries. A special thank for their essential advices and support to Diego Passuello, who first conceived the idea at the basis of this work, and to Giancarlo Cella, who has been kindly available through the formalization of the problem.

Bibliography

[1] P. R. Saulson. *Fundamentals of interferometric gravitational wave detectors*. World Scientific Publishing Co. Pte. Ltd., 1994.

[2] W. Misner, K.S. Thorne, and J. Wheeler. *Gravitation*. W.H. Freeman and Co., 1973.

[3] B.F. Schutz. *Class. Quantum Grav.*, 16:A131–A156, 1999.

[4] L.P. Grishchuk. *Phys. Usp.*, 44:1–51, 2001. http://arxiv.org/abs/astro-ph/0008481.

[5] C. J. Lada. *Astrophys. J.*, 640:L63–L66, 2006.

[6] J.H. Taylor et al. *Nature*, 355:133, 1992.

[7] K. Thorne. LIGO Pac Meeting (2003), Pasadena - LIGO G03029300-R.

[8] A.G. Lyne. *Pulsar Astronomy*. Cambridge University Press, 1990.

[9] T. Regimbau and J.A. de Freitas Pacheco. *Astron. Astrophys.*, 401:385–388, 2003.

[10] M. Gasperini and C. Ungarelli. *Phys. Rev. D*, 64, 2001.

[11] M. Maggiore. *Gravitational Waves*. Oxford University Press, 2008.

[12] L. Barsotti. *Studio dell'acquisizione del controllo dell' interferometro centrale di VIRGO*. Tesi di laurea in fisica, Università degli Studi di Pisa, 2002. http://wwwcascina.virgo.infn.it/theses/.

[13] P. Ruggi. *L'attenuazione del rumore sismico nel rivelatore di onde gravitazionali VIRGO.* Tesi di laurea in fisica, Università degli Studi di Pisa, 2003. http://wwwcascina.virgo.infn.it/theses/.

[14] J.Y. Vinet et al. *Phys. Rev. D*, 56:6085 – 6095, 1997.

[15] J.Y. Vinet, V. Brisson, and S. Braccini. *Phys. Rev. D*, 54:1276–1286, 1996.

[16] J. Hough et al. *The detection of Gravitational Waves.* Edited by D.G. Blair - Cambridge University Press, 1991.

[17] P. La Penna. *Studio di cavità ottiche nell'esperimento Virgo e per misure di rumore termico.* PhD thesis, Università degli Studi di Pisa, 1998. http://wwwcascina.virgo.infn.it/theses/.

[18] F. Acernese et al. *Journal of Physics: Conference Series*, 120, 2008.

[19] A. Brillet et al. *The detection of Gravitational Waves.* Edited by D.G. Blair - Cambridge University Press, 1991.

[20] F. Acernese et al. *Astropart. Phys.*, 30:465–477, 2008.

[21] M. Mantovani et al. *Class. Quantum Grav.*, 23:S91–S102, 2006.

[22] G. Ballardin et al. *Rev. Sci. Instrum.*, 72(9):3643–3652, 2001.

[23] S. Braccini et al. *Astropart. Phys.*, 23:557–565, 2005.

[24] F. Acernese et al. *Astropart. Phys.*, 20:617–628, 2004.

[25] G. Losurdo et al. *Rev. Sci. Instrum.*, 79 (9):3653–3661, 2001.

[26] F. Acernese et al. *Astropart. Phys.*, 20 (6):629–640, 2004.

[27] http://www.virgo.infn.it.

[28] http://www.ligo.caltech.edu.

[29] http://tamago.mtk.nao.ac.jp.

[30] http://geo600.aei.mpg.de.

[31] http://www.icrr.u-tokyo.ac.jp/gr/gre.html.

[32] http://www.gravity.uwa.edu.au.

[33] D.G. Blair. *The detection of Gravitational Waves*. Edited by D.G. Blair - Cambridge University Press, 1991.

[34] http://igec.lnl.infn.it.

[35] P. Astone, J.A. Lobo, and B.F. Schutz. *Class. Quantum Grav.*, 11:2093–2112, 1994.

[36] D. Passuello and S. Braccini. *Correction of Doppler effect by discrete signal resampling* - VIR-046A-07, https://pub3.ego-gw.it/. To be published.

[37] R. E. Ziegler. *Proceedings of the Third Geodetic Symposium on Satellite Doppler Positioning*, 1, 1982.

[38] P. Jaranowski, A. Królak, and B. F. Schutz. *Phys. Rev. D*, 58, 1998.

[39] P. Astone et al. *Class. Quantum Grav.*, 21:S1585–S1594, 2004.

[40] S. Frasca. *The search for Vela Pulsar in Virgo VSR1 data*. 8th Amaldi Conference, 2009.